Universidad Valladolid
Ecole Nationale Supérieure d'Ingénieurs Electriciens de Grenoble (ENSIEG)
Universität Karlsruhe (TH)
Politechnika Gdańska

Modeling and control of the String2 LHC Prototype at CERN

The report on the Master Thesis Project in Control Engineering
written by
Rafal Noga (rafalnoga@hotmail.com)
under supervision of
Prof. Cesar de Prada (prada@autom.uva.es).

See the website of the project: http://www.isa.cie.uva.es/~rafal/

Valladolid, August 31, 2007

Abstract

The Large Hydron Collider (LHC) at CERN will be the newest, largest and highest energy particle accelerator and collider in the world when switched on in May 2008. It consists of more than 1600 superconducting magnets that will be maintained at operational temperature equal to 1.9K by the Superfluid Helium Cryogenic Circuit. This document presents a first principle nonlinear model of the circuit of a LHC Standard Cell to be used in a Nonlinear Model Predictive Control (NMPC) of the superconducting magnets temperature.

First, the CERN, the LHC together with the String Experimental Programme, the Superfluid Helium Cryogenic Circuit and the Nonlinear Model Predictive Control (NMPC) of the circuit are briefly presented.

Then the motivation for the development of the model is explained and the modeling process is presented step by step.

Finally, the extremities of the model of the Standard Cell are connected to models of DFBX and MRB in order to achieve the String2 prototype configuration and the model is adjusted with the experimental data from the String2 experiment. The results of the model simulation are evaluated and the future work is proposed.

Keywords

LHC, Standard Cell, String2 Prototype, Model Based Predictive Control, Cryogenics

Résumé

Le Grand Collisionneur de Hadrons (LHC) du CERN sera le plus récent, le plus grand et équipé des technologies les plus avancées lors de sa mise en service en mai 2008. Il est composé de plus de 1600 aimants supraconducteurs gardés à une température de 1.9 K par un circuit cryogénique utilisant de l'hélium superfluide. Ce document présente le modèle non linéaire d'un circuit d'une cellule standard du LHC qui va être utilisé en commande prédictive non linéaire (NMPC) de la température des aimants supraconducteurs.

D'abord, le CERN , le LHC avec le programme expérimental String, le circuit cryogénique utilisant de l'hélium superfluide et la commande prédictive non linéaire (NMPC) du circuit sont présentés brièvement.

Tout d'abord, nous regarderons l'interêt que présente le développement de ce modèle, ensuite nous expliquerons pas à pas le procédé de modélisation.

Enfin, les parties du modèle de la cellule standard sont connectées avec les modèles de DFBX et MRB pour atteindre le configuration du String2 prototype et le modèle est ajusté avec les données exprimentales de String2 experiment. Les résultats de la simulation du modèle sont valués et le future travail est proposé.

Mots clés

LHC, cryogenique, String2, commande predictive nonlineaire, NMPC

Contents

List of Figures

Chapter 1

Introduction

The Large Hydron Collider (LHC) at CERN will be the newest, largest and highest energy particle accelerator and collider in the world when switched on in May 2008. It consists of more than 1600 superconducting magnets that are maintained at operational temperature equal to 1.9K by the Superfluid Helium Cryogenic Circuit.

The experiments performed on the String and String2 LHC Prototypes from 1995 to 2003 showed that the regulation of the LHC magnets temperature is a challenge, mainly due to presence of strong nonlinearities together with frequent changes of the operation point, inverse response on the control input manipulation and variable dead time of the response.

A PID controller used to control the temperature had poor performance. A MPC controller was developed, tested and showed a great potential to improve the temperature control of the first 53 meter long "Half Cell" String Prototype. Unfortunately the MPC controller could not be commissioned on the 107 meter long "Full Cell" String2 Prototype because of the mismatch between the process dynamics and its model used in the controller.

This document presents development of a new, "first principle" nonlinear model of the Superfluid Helium Cryogenic Circuit of a LHC Standard Cell to be used in a Nonlinear Model Predictive Control (NMPC) of the superconducting magnets temperature.

The model is not complete: the modeling of superfluid helium distribution in the Bayonet Heat Exchanger needs reviewing and the model of the inverse response dynamics has to be closed looped.

This report is organized into three chapters.

This chapter presents general information on the context of the project: the CERN, the LHC together with the String Experimental Programme, the Superfluid Helium Cryogenic Circuit and the Nonlinear Model Predictive Control (NMPC) of the circuit are briefly presented.

Then, in chapter Two, the motivation for the development of the model is introduced, the Superfluid Helium Cryogenic Circuit is described with details and the modeling process of the circuit is presented step by step.

Finally in chapter Three, the extremities of the model of the Standard Cell are connected to models of DFBX and MRB in order to achieve the String2 prototype configuration and the model is adjusted with the experimental data from the String2 experiment. The results of the model simulation are evaluated and the future work is proposed.

The model has been developed in frame of the Master Thesis Final Project under name "Modeling and control of the String2 LHC Prototype at CERN" in time period from March 1, 2007 to August 31, 2007.

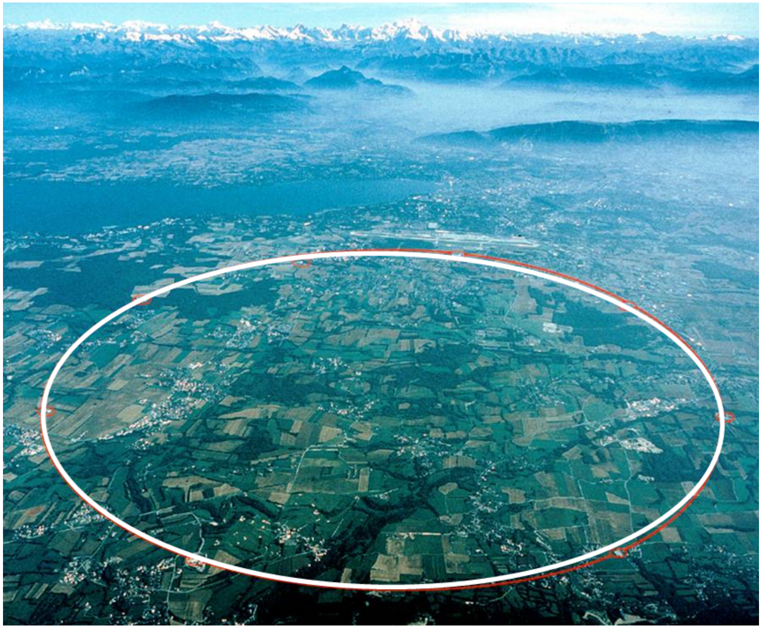

Figure 1.1: The 26.7km circumference of the LHC machine.
(Source: CERN)

1.1 CERN

Founded in 1954, CERN is the European Organization for Nuclear Research, the world's largest particle physics center. It sits astride the Franco-Swiss border near Geneva. CERN currently has approximately 2600 full-time employees mainly from 20 Member Countries.

CERN is a laboratory where scientists study the building blocks of matter and the forces that hold them together. CERN exists primarily to provide them with the necessary tools. These are accelerators, huge machines able to speed up particles to very high energies before smashing them into other particles.

By accelerating and smashing particles, physicists can identify their components or create new particles, revealing the nature of the interactions between them [1].

Some 7931 scientists and engineers representing 500 universities and 80 nationalities work on experiments conducted by CERN [3].

1.2 Large Hydron Collider (LHC)

The Large Hadron Collider (LHC), with its 26.7km circumference and 14 TeV of collision energy, will be the newest, largest and highest energy particle accelerator and collider in the world when switched on in May 2008. See Fig. 1.1.

With its collision energy seven times higher than that of any other proton accelerator to date, LHC will probe deeper into matter than ever before [1].

It is hoped that the collider will produce the elusive Higgs boson particle, often dubbed the God Particle, the observation of which could confirm the predictions and 'missing links' in the Standard Model of physics, and explain how other elementary particles acquire properties such as

Figure 1.2: LHC machine in the tunnel.
(Source: CERN)

mass.

Six experiments (CMS, ATLAS, LHCb, TOTEM, LHC-forward and ALICE) are currently being built, and will be running on the LHC. [2]

1.2.1 Accelerator construction

The accelerator consists of a vacuum chamber surrounded by long sequence of vacuum pumps, magnets, radio-frequency cavities, high voltage instruments and electronic circuits.

The vacuum chamber is a metal pipe where air is permanently pumped out to make sure the residual pressure is as low as possible. Inside the pipe, particles are accelerated by electric fields.

Powerful amplifiers provide intense radio waves that are fed into resonating structures, the Radio-Frequency (RF) cavities. Each time the particles traverse a RF cavity, some of the energy of the radio wave is transferred to them and they are accelerated.

To make a more effective use of a limited number of RF cavities, accelerator designers force the particle beam to go through them many times, by curving its trajectory into a closed loop. That is why the LHC looks roughly circular.

Curving the beam's path is usually achieved by the magnetic field of dipole magnets. The higher the energy of a particle, the stronger magnets are needed to create the bending field.

In addition to just curving the beam, it is also necessary to focus it. Focusing the beam allows its width and height to be constrained so that it stays inside the vacuum chamber. This is achieved by quadruple magnets, which act on the beam of charged particles exactly the same way a lens would act on a beam of light.

In the LHC two counter-rotating proton beams will circulate in separate vacuum chambers installed in the same magnets ('twin-aperture' magnets) [1].

1.2.2 Standard Cell

Standard Cell is a basic construction structure of the LHC. Each 106.9 meters long Standard Cell comprises 6 dipole magnets (32 tons and 15 meters in length) and 2 Short Straight Section (SSS), each housing one quadropole magnet (8 tons - length 6 meters).

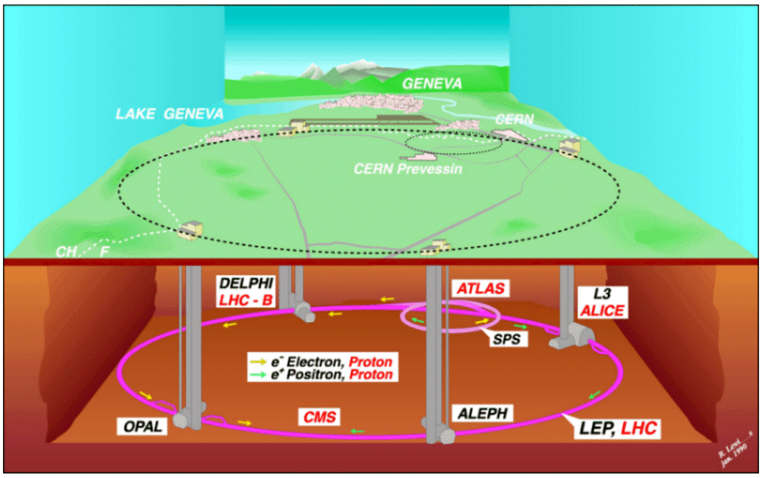

Figure 1.3: LHC machine localization.
(Source: CERN)

23 standard cells are connected together to build one 3.3km long LHC arc. 8 such arcs are constitutes the 26.7km circumference ring of the LHC machine that is hosted in a tunnel at about 100m underground, see figures 1.1, 1.3 and 1.2.

1.2.3 Superconducting devices

Superconductivity is a phenomenon occurring in certain materials at extremely low temperatures, characterized by exactly zero electrical resistance and the exclusion of the interior magnetic field (the Meissner effect). The resistance of a superconductor drops abruptly to zero when the material is cooled below its "critical temperature". An electrical current flowing in a loop of superconducting wire can persist indefinitely with no power source [4].

The basic functions of beam guiding, focusing and accelerating in the LHC are performed by superconducting devices - magnets and RF cavities. The strong magnetic fields of the LHC devices require large electric currents of several thousands amperes the only way to achieve high performance with low energy losses is by reducing the electrical resistance by using superconductivity.

The LHC is the largest project to use superconducting magnets and the largest superconducting installation in the world: more than 1600 magnets create the 26.7km circumference of the LHC machine.

1.2.4 Cryogenic System

The LHC superconducting (NbTi windings) magnets need to be cooled with superfluid helium at 1.9 K (colder than outer space) in order to maximize its operational magnetic field curving the beam.

That is why the large-scale helium cryogenics has become a key technology in accelerator construction and operation. The total mass of 36.8×10^6kg of equipment will be cooled down. Total inventory of liquid helium during the operation of LHC will be around 700,000 litres. To supply the cooling power to strings of magnets, eight helium liquefier stations of refrigeration power 18 kW (at 4.5 K) each will be located at several points along the accelerator.

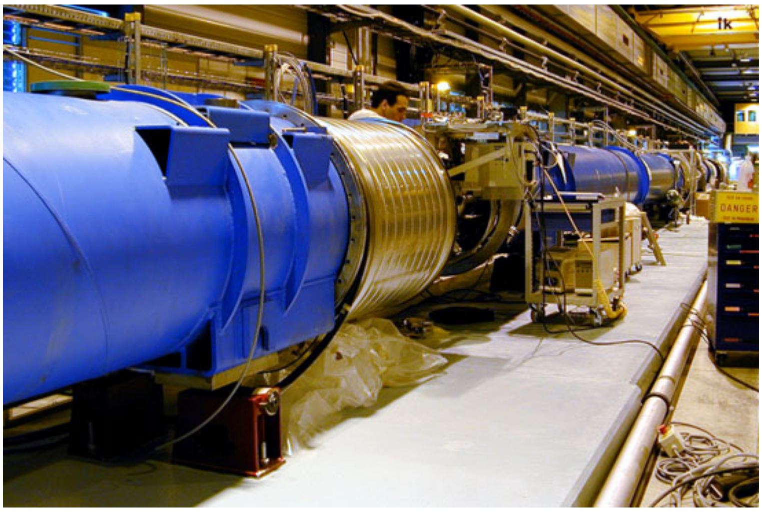

Figure 1.4: String2 Prototype.
(Source: CERN)

1.2.5 String Prototypes

An intensive R&D was crucial for the successful construction of the LHC. At the end of 1994, an important milestone of the LHC R&D programme was reached with the first operation of an entire prototype section of the accelerator - the String Prototype. This full-scale model representing a half-cell of the machine lattice was operated and extensively tested until 1999.

Following the successful results of the String Prototype, a new "full-cell" model - the Test String 2 - has been designed, assembled and commissioned.

It has been operated since 2001 until 2003 in three main successive phases. During the first phase, the facility, which comprised an electrical feed box, a half-cell and an additional short straight section, was assembled using exclusively prototype components specially instrumented for the experimental programm. For phase 2, three pre-series dipole magnets were added thus completing a 107-m length full cell of LHC. The three dipoles were machine worthy pre-series magnets.

In its phase 3 String 2 was modified to represent more closely the LHC Standard Cell, with the aim to assess its thermal performance at 1.9 K. A large amount of excess instrumentation was removed and repairs were made to the thermal shielding. See Fig. 1.4

Combined, the two operational models ran, from 1995 to 2003, under machine-like conditions for more than 20'000 hours, representing more than 3 years of continuous operation of the LHC collider.

The String Prototypes have been extremely valuable tools to validate cryogenic components and design choices, investigate the collective behavior and operational scenarios, improve the process and operating conditions, and finally, train future operating crew of a complex machine as the LHC prior to installation in the underground tunnel.

Until now they are also the unique source of experimental data of the LHC Standard Cell Superfluid Helium Cryogenic Circuit.

1.3 Superfluid Helium Cryogenic Circuit of a Standard Cell

Superfluid Helium Cryogenic Circuit of the LHC Standard Cell (called also 1.9K Cooling Loop) is in the center of interest of this project. It is a very interesting circuit because it uses as coolant superfluid helium exhibiting extraordinary physical properties. It is also a difficult circuit to control because of the presence of the superfluid helium exhibiting highly-nonlinear characteristics and strict operational constraint imposed by operational conditions of the superconductive magnets.

1.3.1 Helium at low temperatures

Helium-4 at temperatures in range of 1.9 - 4.5K and pressures between 16×10^3 and 3 bar is used in the cooling loop. That means that helium appears either in liquid and superfluid phase.

The transition from one phase to another occurs at λ point, $T_\lambda \simeq 2.17K$ - depending on pressure.

At the temperatures above the λ point, helium is in the liquid phase - Helium I, having the same properties as other liquids. Below the λ point helium becomes a superfluid Helium II with vanishing apparent flow resistance through narrow capillaries and anomalously high heat transport capability. Both properties are of interest for cooling applications because they imply high heat removal potential in conjunction with little pumping work at cryogenic temperature. [15]

The density of liquid helium is quasi constant in wide range of pressures and temperatures:

$$\rho_l = 0.146kg/l$$

1.3.2 Purpose

The task of the Superfluid Helium Cryogenic Circuit of a LHC Standard Cell is to provide cooling needed to keep in superconducting state the NbTi magnet windings of the 8 magnets comprised in the Standard Cell.

The NbTi windings exhibit superconductive properties only in very low temperatures about 2K and they lost it when their temperature overrides a specific level, being a function of the intensity of the magnetic field. That is why the cooling of the windings is needed.

1.3.3 Operation principle

The superconducting magnet windings are completely submerged in a bath of pressurized helium. The heat created in magnet windings is transported via winding insulation to the helium bath. The pressurized superfluid helium is chosen to be the coolant because of its extraordinary cooling properties: small viscosity (great penetrating abilities), large specific heat and great thermal conductance.

Heat flows into the helium bath also from other magnet components, like for example: from iron yoke, originating in the energy dissipation by magnetization losses, from the beam screen caused by beam dissipation on the beam screen walls or leaking from outside via thermal insulation.

In order to avoid the resistive transition in the superconducting magnet windings, that appears at about 2.3K, the temperature of the helium bath must be kept at 1.9K by moving away the heat from the bath. This is done by Bayonet Heat Exchanger (BHX) with evaporating saturated He II as coolant. BHX is the main element of the cooling loop.

Figure 1.5 presents cryogenic flow scheme and instrumentation of the LHC Standard Cell. In this figure the BHX is drawn as the horizonal tube passing through all the eight magnets. The magnets are signed as Q - quadropole and D - dipole magnets.

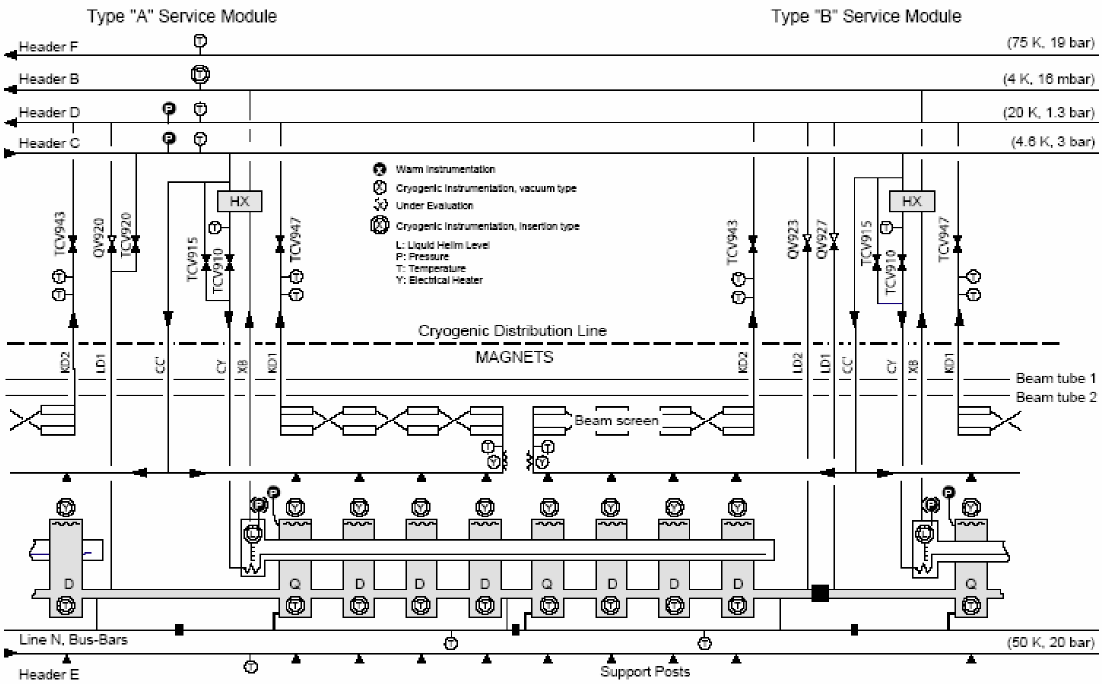

Figure 1.5: Cryogenic flow-scheme and instrumentation of a LHC lattice cell. (Source: [27])

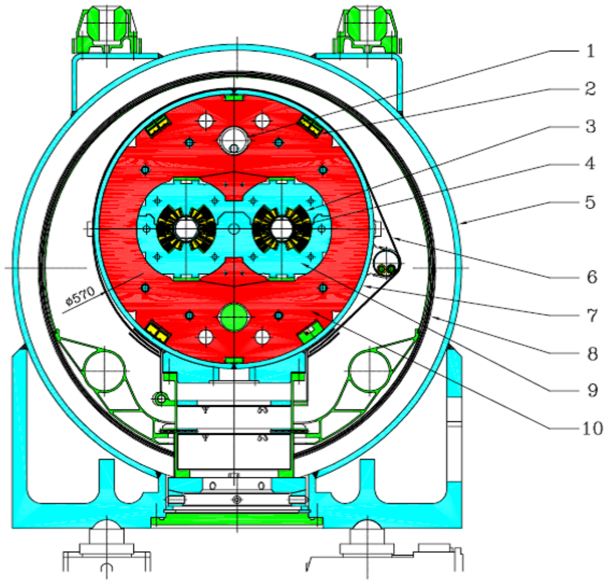

Figure 1.6: Cross-section of the LHC Magnet.
1 =heat exchanger pipe,2 =superconducting busbars, 3= superconducting coils, 4= beam screen, 5 =vacuum vessel, 6 = radiation screen, 7 =shrinking cylinder (He II vessel), 8= thermal shield (55 to 75 K), 9= non-magnetic collars, 10 = iron yoke (cold mass at 1.9 K)(Source: CERN)

The liquid helium to be used in the BHX is taken from the header C at 4.6 K and 3 bar. This pressurized He I is cooled down to 2.2K in a very low pressure (VLP) heat exchanger (HX in the fig. 1.5) in counterflow with 1.8 K, 16mbar helium vapor coming from the BHX (line XB in the scheme).

After cooling down the pressurized He II at 2.2K, 3bar is expanded to about 16mbar via a the Joule-Thompson (J-T) valve (TCV910) and the small diameter feeding pipe (FP) placed inside the BHX.

A Joule-Thomson (JT) valve, is a valve used widely in cryogenics that allows helium to expand, normally used to liquify a gas, but this is not a case in the circuit because liquid helium is expanded through the valve, and all liquids warm up during the expansion.

During this expansion, helium pressure falls to the values smaller than the vapor pressure of helium at a given temperature. This makes the helium evaporate cooling itself down to the saturation temperature.

The FP length is about 100 m and it deposits both the saturated helium and the vapor to the opposite end of the BHX.

Then, the saturated He II and helium vapor flow in opposite direction, from the end of the FP in direction to the JT valve, through the 100 meter long BHX and evaporate as a consequence of the heat flow from He bath to the saturated He II. The amount of the superfluid helium evaporating in the BHX, thus the amount of heat that it can absorb, is regulated via JT valve position.

The BHX is sized to work as partially wetted. This means that in nominal conditions the helium flowing in the exchanger evaporates completely before reaching the opposite end of the BHX. The vapor at about 1.8 K created in the BHX is pumped out to the Header B in order to keep the low vapor pressure (16 mbar) in the BHX. The pressure in the BHX determines

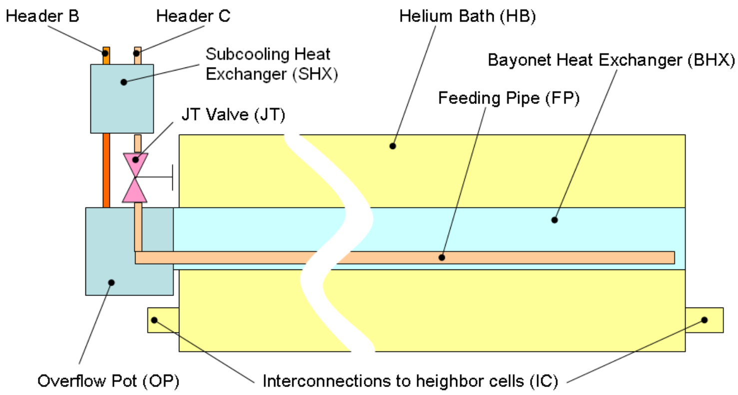

Figure 1.7: Simplified scheme of the Standard Cell Cryogenic Circuit

the saturation temperature of superliquid helium flowing through the BHX, thus the minimal achievable temperature of the helium bath.

Before the vapor reaches the very low pressure pumping header B it passes throw the subcooling heat exchanger (SHX) (symbol HX in the figure 1.5) where it cools down the pressurized helium flowing from Header C.

An additional JT valve CV915 by-passing the warm heat exchanger is used only for cooldown or in case the heat exchanger is clogged.

The description is illustrated with simplified schemes: see figures 1.7, 1.8 and 1.9.

1.3.4 Operational constraint

The superconductivity in the NbTi windings disappears when the temperature, the applied magnetic field or the current density exceeds material dependent critical values e.g. 2.3K at nominal field of 8.33 T and 14kA of conducting current.

The superconducting material has to be operate with a safe margin to the temperature of resistive transition - so-called current sharing temperature. Taking into account the thermal resistance of the winding insulation the temperature of the pressurized superfluid helium (He II) surrounding the windings cannot exceed a specific level placed slightly above the operational point equal 1.9 K. This is the strict operational constraint of the superfluid helium circuit.

Failure consequence: quench

The quench is what happens when the Superfluid Helium Cryogenic Circuit fails or from any other reason the temperature of the NbTi windings overrides the specific temperature level causing the resistive transition of the NbTi windings from the superconducting to the normal-conducting state.

In the first few tenths of a second following the transition of a dipole magnet, the $500\frac{kJ}{m}$ stored magnetic energy is dissipated in, now, resistive magnet windings heating the pressurized helium and causing its pressure and the temperature to rise what could cause an explosion.

Security systems, fired as soon as quench takes place, and quench recovery circuits have been constructed to minimize the effects of this explosion, therefore quench in one of more than 1600 superconducting magnets will interrupt the machine operation for 2 - 6 hours, time needed to re-cool-down of limited stretches of magnet after a resistive transition.

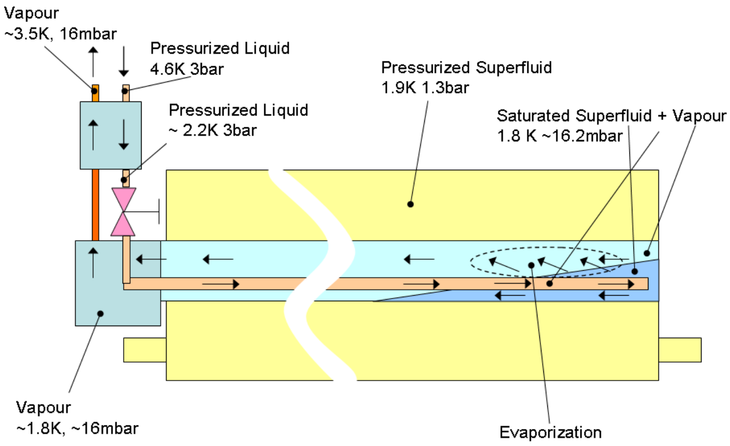

Figure 1.8: Simplified helium flow in the Standard Cell Cryogenic Circuit

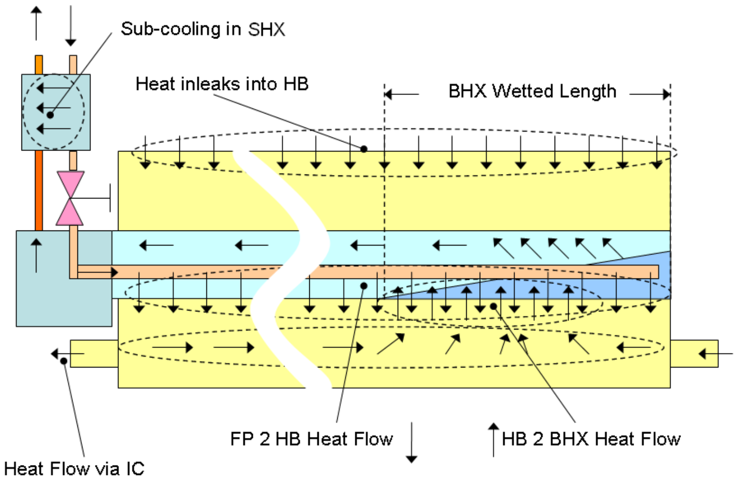

Figure 1.9: Simplified energy flow in the Standard Cell Cryogenic Circuit

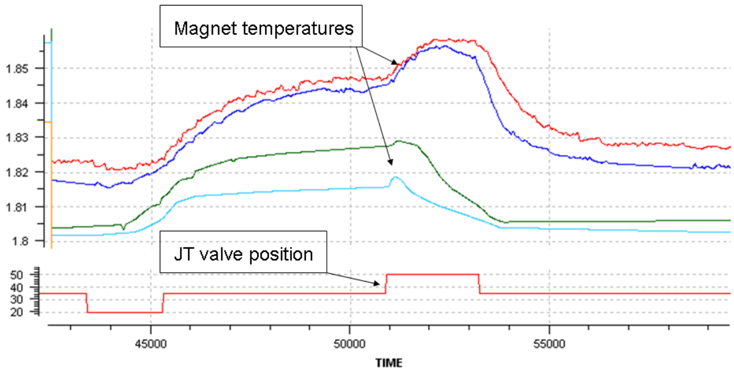

Figure 1.10: The dynamics of the superfluid circuit.
The four curves above are magnet temperatures, the lowest is the position of JT valve.

1.3.5 Experience with magnet temperature regulation

The temperature of the helium bath depends on the cooling capacity of the BHX that is a function of the amount of evaporating helium in the BHX that is controlled by the JT valve position.

The temperature of the bath is measured in 8 points along the Standard Cell corresponding to for each magnet position.

Thanks to the String Experimental Programme a lot of experience about operation of the cryogenic circuit has been gained. Unfortunately, the temperature regulation of the superfluid circuit turned out to be a difficult problem mainly for two reasons.

First, the circuit exhibits complicated dynamics including: asymmetric inverse response of the bath temperature on a JT valve manipulation, where temperature excursion varies in function of its direction, variable dead-time depending mostly on the heat load situation, and non-uniform magnet temperature across the string of magnets due to a constrained longitudinal heat transfer. [5] The time evolution of the magnet temperatures in four points along the String2 as the effect of change in the JT-Valve opening is presented in the figure 1.10.

Second factor making the control difficult is the weak long time stability and high failure rate of the temperature sensors working in hard conditions at 1.9K.

Standard PID (Proportional Integral Differential) control has been applied in the past in order maintain the magnet temperatures at a given set point. While being able to operate the plant, the PID controller showed poor performance when perturbations or changes of the operating conditions (mainly changes of static heat load into the HB) took place.

That is why an advanced control strategy such as the Model Predictive Control has been developed, commissioned and tested on the first String Prototype. The observed performance of the MPC controller was very good [6].

As an effect of the simplification of the Cryogenic Distribution Scheme for the Large Hadron Collider proposed in 1996 [7, 5], the length of a Superfluid Helium Cryogenic Circuit of the LHC Standard cell doubled to reach 107m.

Unfortunately the type of models used before to describe the dynamics of the system turned out to be inadequate to model the new, much longer Standard Cell. As an effect, the MPC controller could not be commissioned on the 107 meter long "Full Cell" String2 Prototype because of the mismatch between the process dynamics and its model used in the controller.

1.4 Nonlinear Model Predictive Control (NMPC) of the superconducting magnet temperature

In this section the motivation for the development of the NMPC for the Superfluid Circuit is presented and followed by a short introduction into the principle of NMPC. Then the key elements of the implementation of the NMPC to the superconducting magnet regulation is presented and finally the actions that have to be performed to succeed the implementation are listed.

1.4.1 Motivation for the development of the NMPC for the Superfluid Circuit

Encouraged by the very good results of the MPC advanced control of the magnet temperature on the first 53.5 m long String Prototype an attempt was made to use the the advanced controller in the 107 m long LHC Standard Cell.

The experiments with the 107m long String2 Prototype showed that its thermal dynamics cannot be anymore approximated as linear in order to design a predictive controller. The nonlinearities of the system have to be taken into account and a Nonlinear Model Predictive Controller (NMPC) must be developed.

The motivation to develop the NMPC is strong because the experiments with the String2 Prototype showed how difficult and sensitive to changes of a operation point (caused by changing static heat load into the magnet cold mass) is the tuning of a PID controller.

Inefficient performance of the PID control of the superconducting magnets temperature causes higher risk of exceeding the maximal magnet temperature causing quench that stops the whole LHC machine.

A supplementary benefit of use of advanced controller can be reduction of requirements on the thermometers accuracy and thus extending the periods between the thermometer calibration.

Summarizing the successful realization of a NMPC controller of the superconducting magnet will extend the time in which the LHC will be available for experiments.

1.4.2 Introduction into Nonlinear Model Predictive Control (NMPC)

The nonlinear model predictive control (NMPC) is a successor of the linear model predictive control (MPC) that is popular since the 70s of the past century.

Citing the introduction to the NMPC written by Rolf Findeisen and Frank Allgoewer [8]:
In general, the model predictive control problem is formulated as solving on-line a finite horizon open-loop optimal control problem subject to system dynamics and constraints involving states and controls. Figure 1.11. shows the basic principle of model predictive control. Based on measurements obtained at time t, the controller predicts the future dynamic behavior of the system over a prediction horizon T_p and determines (over a control horizon T_c) the input such that a predetermined open-loop performance objective functional is optimized. If there were no disturbances and no model-plant mismatch, and if the optimization problem could be solved for infinite horizons, then one could apply the input function found at time t = 0 to the system for all times $t \geq 0$. However, this is not possible in general. Due to disturbances and model-plant mismatch, the true system behavior is different from the predicted behavior. In order to incorporate some feedback mechanism, the open-loop manipulated input function obtained will be implemented only until the next measurement becomes available. The time difference between the recalculation/measurements can vary, however often it is assumed to be fixed, i.e the measurement will take place every d sampling time-units. Using the new measurement at time t + δ, the whole procedure prediction and

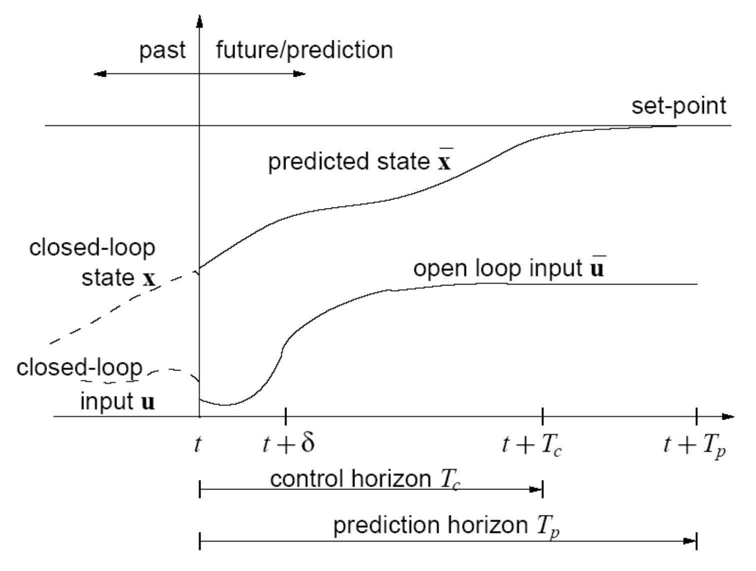

Figure 1.11: Principle of model predictive control.
(Source: [8])

optimization is repeated to find a new input function with the control and prediction horizons moving forward.

The overall basic structure of a NMPC control loop is depicted in Figure 1.12. As can be seen, it is necessary to estimate the system states from the output measurements.

NMPC found many implementations in control of slow industrial processes because this are in general nonlinear, multivariable processes operating under constraints and the NMPC handles nonlinear dynamics, multivariable systems and constraints in easy way. The only restriction on implementation possibilities of NMPC is imposed by the time needed to perform a complex optimization calculations in order to solve a NMPC problem - the NMPC can be used only to control relatively slow processes.

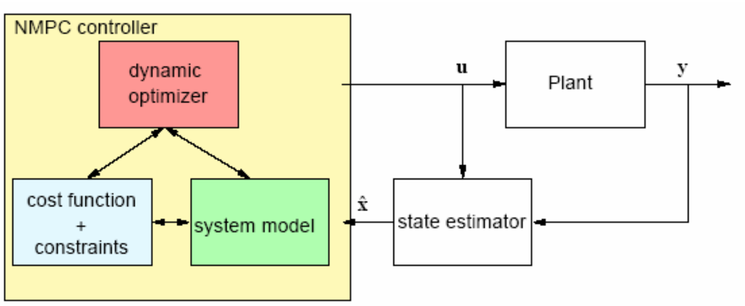

Figure 1.12: Basic NMPC control loop.
(Source: [8])

1.4.3 Realization of the NMPC to the regulation of magnet temperatures

The implementation of the NMPC to the regulation of magnet temperatures starts at logical level with the development of the process model and the NMPC algorithm that computes the optimized control input (JT valve position) basing on the predicted future system responses available after online simulation of the process model.

Then the physical layer needs to be developed. The physical implementation of the NMPC is similar to the existing implementation of the PID control. The main difference between them is that the the NMPC needs much more computing power to run the optimization algorithms what implies an introduction of additional industrial computers.

There are no difference between the physical realization of the MPC and NMPC control, so all the infrastructure already designed for the MPC can be reused. The main effort to succeed the realization of the NMPC control of magnet temperatures is related to the design of the logical layer including the NMPC algorithm and a nonlinear model of the temperature dynamics of the system.

Chapter 2

Modeling the Superfluid Helium Circuit of a Standard Cell

A nonlinear model of the Superfluid Helium Circuit of a Standard Cell has to be developed in order to realize the advanced control of the superconducting magnets temperature. Additionally, the model can be used to improve the fault detection in the circuit.

2.1 Specification of the model

Specification for the model is imposed by needs and available resources.

2.1.1 Purpose

The purpose of the model is to calculate future values of the temperature of the Standard Cell Helium Bath as the function of the present state of the circuit, future control inputs and predictable disturbances.

2.1.2 Speed and precision of the simulation

The results of calculation of future value of the maximal temperature of the Helium Bath are useful to the online optimization of the control signal by the NMPC algorithm only if the calculation of the variable is performed much faster than its real evolution. In this case the NMPBC optimizer is able simulate the behavior of the system many times for different control inputs before choosing the optimal one. The speed of simulation is a stiff constraint by the model design, with a slow model no NMPC is possible.

The best achievable performance of the NMPC controller is determined by the precision of the model.

The dynamics of the Superfluid Circuit is quite complicated, with many nonlinear relations so probably it wont be possible to create a precise model that can be simulated enough fast for the NMPC algorithm. In this case some simplifications have to be made to the model in order to achieve the satisfying speed of simulation. This simplifications will cause loss of the model precision and as result degradation of the NMPC performance.

2.1.3 Nonlinear model

The model has to represent all crucial circuit nonlinearities that caused malfunction of the PID and linear MPC control strategies in presence of significant changes of the operation point of the Prototype that has been observed during the String experiments.

The problem with the linear modeling of the String2 Superfluid Helium Circuit is that the linear model of the system is valid only in very small area close to the linearization point because the presence of strong system nonlinearities and cannot cover the wide space of operation points that has been observed during the experiments.

2.1.4 Black box and first principles model

No experimental data from the Standard Cell is available until today. The available data comes from the String2 Prototype.

Unfortunately, even if the construction of the prototype is very similar to this of the Standard Cell, the presence of significant differences of thermal performance between the process and its prototype (due to absence of interconnections to the other cells in the prototype) excludes the possibility of black-box nonlinear modeling using nonlinear identification.

On the other hand the experimental data from the String Prototype together with its technical specification can be used in successful development of a first principles model.

For this reason the following part of this paper will describe the modeling of the Superfluid Helium Circuit by exact or approximated mathematical description of the processes present in the circuit - a first principle model of the Superfluid Helium Circuit will be developed.

2.1.5 Inputs/outputs

The temperature values along the LHC Full Cell Helium Bath have to be calculated and its maximal value will be selected as the output value of the model.

The control input is the position of the JT valve that determines the amount od helium evaporating in the BHX thus its cooling power.

The main predictable disturbances that can be treated as inputs are: pressure changes in the Header B that influence the temperature and cooling power of the BHX and dynamic head loads into the HB correlated to operation of other Standard Cell circuits. The inputs can be used to realize feed-forward control if predicted values of the disturbances are available.

Other input variable of the model is the static heat load into the superfluid circuit that defines the operation point of the circuit. Its value can be estimated from the dynamics of magnet temperatures and the JT valve position.

The heat flows through the interconnections to neighbor cells are important inputs/outputs of the model that make possible a simulation and predictive control of the helium bath temperature of a Standard Cell interconnected to other cells.

In the LHC machine, 23 interconnected cells compose an 3.3km long LHC arc.

2.1.6 Model operation limits: $T_{H;max}$

The model must be able to simulate a LHC Standard Cell working at normal operation conditions. There are no significant changes in physical mechanisms governing the circuit dynamics as long the pressurized helium in the HB is in superfluid state. That is why I assumed the maximal operational temperature of the HB in the model

$$T_{H;max} = 2.15K$$

that is slightly below the λ point.

2.1.7 Modeling language - EcosimPro4^R

The model has been developed using EcosimPro4 software.

EcosimPro^R is a simulation tool with an user-friendly environment developed by Empresarios Agrupados International for modeling simple and complex physical processes that can be expressed in terms of differential-algebraic equations or ordinary-differential equations and discrete events.

The modeling of physical components is based on the EcosimPro^R language (EL) which is very similar to other conventional programming languages but is powerful enough to model continuous and discrete processes. [9]

EcosimPro4^R modeling language offers some advantages for modeling physical systems, among them the facilities for true reuse of models in different contexts.

In addition the software automatically generates C++ code that can be directly used for control purposes.

2.2 Previous work

The project is a continuation of work of several people.

Cesar de Prada and Enrique Blanco have created good models for of temperature dynamics of the Superfluid Helium circuit of a "half-cell" [6] and the Inner Triplet that are shorter than the full-cell. They have also worked on a model of the Full-Cell and this project base on the results of their work.

Before them, Bjrn Flemster [10]and Jrn Andersen [11] also developed superfluid helium circuit models of a "half-cell".

2.3 Helium properties data from HEPAK

All data about properties of helium used in the Superfluid Helium Circuit come from HEPAK v3.4.

Citing the HEPAK User's Guide [12]:

> HEPAK is a computer program for calculating the thermo-physical properties of helium from fundamental state equations. The state equations are valid from 0.8 Kelvin or the melting line to 1500 Kelvin, including the superfluid range, the lambda line, and liquid vapor mixtures; as a function of pressure they are valid up to 1000 bars, except between 80 and 300 Kelvin where they are valid to 20,000 bars. HEPAK also includes thermal transport properties in both normal and superfluid, the dielectric constant, refractive index, and fluid surface tension.

2.4 Temperature of the pressurized He II Bath (HB)

The purpose of the project is to find a link between the value of the maximal temperature of the LHC Full Cell Helium Bath (HB) and the model inputs.

The HB is composed of pressurized helium that completely feel the free space inside the magnets surrounding all magnet components. This configuration improve stability of the magnet windings temperature, due to large value of specific heat of HeII and the performance of heat evacuation from the magnet thanks to the great thermal conduction of the superfluid helium, peaking at 1.9K and its small viscosity effecting in its great penetration abilities inside the magnet construction.

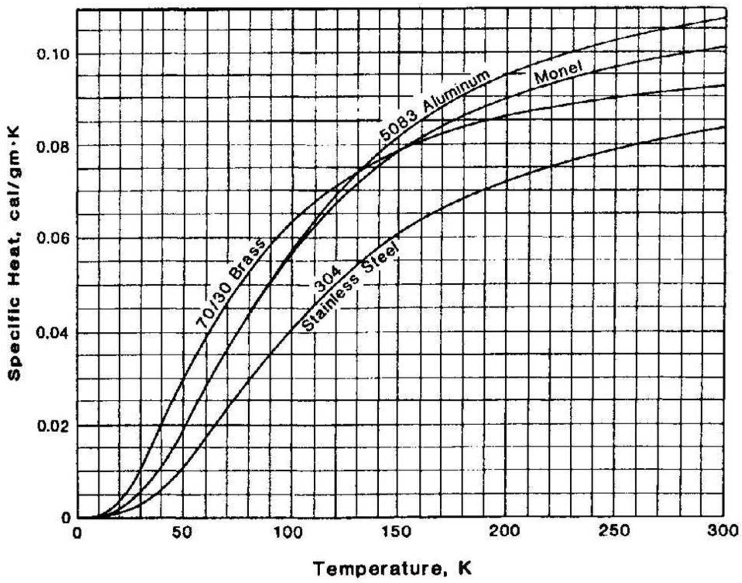

Figure 2.1: Specific heat capacity of metals at low temperatures.
(1 cal = 4.18 J) Source: [13]

2.4.1 Simplifications

Important simplification regarding HB has been made in order to accelerate model computations without significant precision degradation.

Neglecting the specific heat capacity of magnet cold components

The value of the specific heat capacity of the superfluid helium, peaking at 2.17K, see figure 2.2, is many thousands times larger than the specific heat of the magnet components made from metal, that is practically equal 0 for the temperatures below 10K, [13], see figure 2.1

Even when the mass of helium in the Standard Cell, about 320 kg, represents only 0.2% of the mass the Standard Cell, equal about 160 000 kg, the disproportion of the values of the specific heat capacities causes that the major part of the internal energy of the Standard Cell is accumulated in the superfluid helium.

That is why the specific heat of the massive cold magnet components has been neglected in the calculation of the magnet temperature and the presence of their huge mass is introduced as a correction to the value of the superfluid helium mass present in the HB.

Neglecting heat transfers inside metal magnet components

The internal heat transfers inside all magnet components surrounded by the pressurized HeII are neglected.

This is justified by a much larger value of heat conductance of superfluid helium than other magnet components and its very small viscosity, enabling the helium to penetrate deep into the magnet structure.

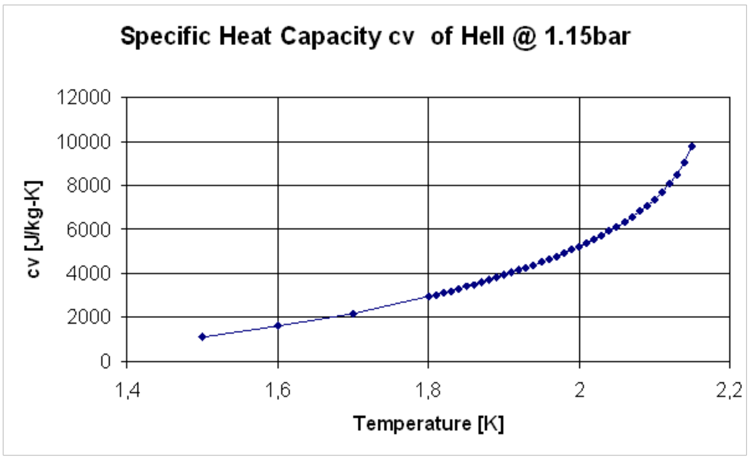

Figure 2.2: Specific heat capacity of HeII @ 1.15 bar. Source: HEPAK

Equal temperatures of magnet and HB

The dynamics of the heat transfer between the magnet cold components and the superfluid helium have been neglected.

The reason for this is that helium has much larger value of the specific heat than other components, thus the dynamics of helium temperature is much slower than the dynamics of the temperature of other magnet components.

Additionally, the superfluid penetrates deep into the magnet components due its small value of viscosity creating a large contact surface thus the thermal resistance between the superfluid helium and magnet components is very small.

In effect the dynamics of the heat transfer between helium and other magnet components can be neglected, thus the measured magnet temperature is always equal to the the temperature of the HB.

One-dimensional problem

The HB has large length-to-diameter ratio greater than 100 so that the problem can be considered one-dimensional.

No longitudinal convection of helium

Other simplification is assumption that the HB is static and no longitudinal superfluid convection occurs in the HB. This assumption means that the heat in the HB is transported only by diffusion what significantly simplifies the simulation.

Equal distribution of helium

First, the interconnections between the HB of each magnet in the Standard Cell has been neglected in modeling and the helium bath is modeled as one 107m long bath of helium with constant cross-section. The reason for this is that the String experiments showed that the increased temperature split over the interconnection is smaller than over the first dipole. Hence the interconnection does not constitute a considerable thermal resistance compared the to the cold masses. This also applies

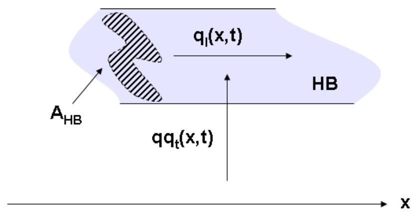

Figure 2.3: Illustration to the energy conservation equation of the HB.

for the transient period of the experiment where the largest temperature split was observed over the length of the first magnet and not over the interconnection.

Second simplification, the simplification that the pressurized helium is equal distributed over whole length of the HB can possibly introduce the considerable error into the model without having any influence on acceleration of the simulation. It is clear that the distribution of pressurized HeII is different in a quadropole than in a dipole because the construction of the different magnet types are different. Unfortunately, I have found only data describing total inventory of pressurized helium in a Standard Cell so I had to unify the helium distribution over the HB length.

2.4.2 Distributed model

The 107m long HB has to be modeled as distributed because the existence of the non-uniform cold mass temperature along the full cell has been observed during experiments on the Test String2.

This non-uniformity corresponding to the existence of non negligible thermal impedance in the magnets and/or interconnections probably will determine the value and position of the maximal He II bath temperature in case of multiple interconnected full cells.

2.4.3 Energy conservation equation

Taking into account the simplifications presented above, the dynamics temperature of the distributed HB can be expressed with a partial differential equation (PDE).

Assuming that the density of the superfluid helium is constant in the operational range of temperatures of the model 1.5 - 2.15K, the pressure of the helium present in the constant volume of the magnet does not change. I this case the change of the helium bath enthalpy $H_H(x,t)$, that is equal to the change of system internal energy:

$$\frac{\partial(\rho_{He}H_H(x,t)}{\partial t} = (\frac{\partial q_l(x,t)}{\partial x} + \frac{qq_t(x,t)}{A_H}) \tag{2.1}$$

+ certain boundary conditions

The equation is illustrated by the figure 2.3

The symbol A_H represents the cross-section area of the pressurized HeII of the HB, ρ_{He} stands for the helium density.

A nonstandard symbol in the equation 2.1 is $qq_t(x,t)$ standing for the transversal heat flow per unit length ($\frac{W}{m}$), $q_l(x,t)$ is the longitudinal heat flux per unit area in $\frac{W}{m^2}$.

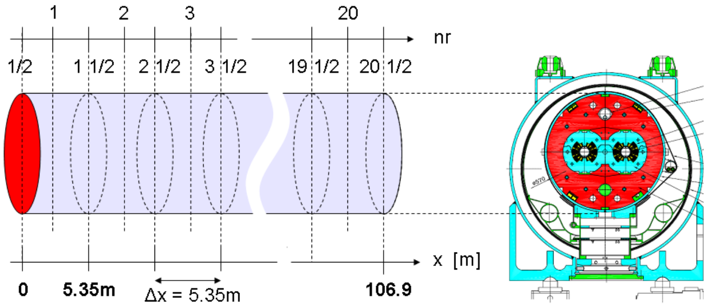

Figure 2.4: Discretization of the HB.

The temperature of the HB $T_H(x,t)$ is a function of its enthalpy, and assuming the constant pressure of the HB equal 1.15 bar can be found easily interpolating discrete values of the $T = f(H)@1.15bar$ from HEPAK:

$$T_H(x,t) = f(H_H(x,t)) \tag{2.2}$$

2.4.4 Discretization

The problem formulated in the equation 2.1 can be solved numerically only after time and spatial discretization. The spatial discretization will convert the partial differential equation into a set of standard differential equations. This set of equations can be solved after time discretization.

The simulation step equal to the period of time discretization will be chosen automatically by the EcosimPro4 simulation environment in order to get right precision of numerical integration.

The period of spatial discretization will define the structure of the model and has to be defined first. Base on experience from model simulation I chosen $\Delta x = 5.35m$ as giving a good compromise between the speed nd precision of simulation.

This means that 107m long HB has been divided into 20 sectors, each 5.35m long, see Fig. 2.4

After the discretization the PDE 2.1 becomes a set of 20 Ordinary Differential Equations (ODE):

$$\frac{d(H_{H,i}(t)m_{H,i})}{dt} = \sum Q_i(t); i \in < 1...20 > \tag{2.3}$$

and

$$T_{H,i} = f(H_{H,i}); i \in < 1...20 > \tag{2.4}$$

For each sector i three elements must be found in order to find the temperature of the helium in the sector $T_{H,i}$: the relation between enthalpy and temperature $T_{H,i} = f(H_{H,i})$, the corrected mass of helium in the sector $m_{H,i}$ and the sum of all heat transfers through sector walls $\sum Q_i(t)$.

2.4.5 Model output: magnet temperatures

The output of the model are 8 values of the HB temperature at coordinates corresponding to the position of the temperature sensors in the Standard Cell.

I have not found a complete Standard Cell documentation, so I do not know exactly where the sensors are. Juan Casas from CERN told me that they are approximately in the middle of each magnet.

I found following vector of magnet positions (for the calculus see the Appendix A.1) :

$$x_M = [3.31; 14.42; 30; 45.65; 56.76; 67.87; 83.48; 99.1][m]$$

The values of the HB temperature at these points must be interpolated using the values of the temperature at the closest discretization point and the gradients $\frac{dT_{H;i+1/2}}{dx}$

$$T_{M;i} = T_{H;j} + \frac{dT_{H;i+1/2}}{dx}\left(x_{M;i} - x_{H;j}\right) \tag{2.5}$$

The discretization points lying closest to the magnet positions are numbers

$$j = 1, 3, 6, 9, 11, 13, 16, 19$$

and their position :

$$x_H = [2.6725; 13.3625; 29.3975; 45.4325; 56.1225; 66.8125; 82.8475; 98.8825][m]$$

The gradients of temperature are calculated as follows:

$$\frac{\partial T_{H;i+1/2}}{\partial x} = \frac{T_{H,i+1} - T_{H,i}}{\Delta x} \tag{2.6}$$

where Δx is the interval of spatial discretization corresponding to the HB sector length.

2.5 Enthalpy of pressurized HeII

The relation between the enthalpy and temperature of the HB must be found in order to solve the equation 2.4.

The HB is concerned as assembly of cold magnet mass and superfluid helium where the energy is stored mainly in the superfluid helium due to its large specific heat coefficient.

That is why I used the values of the enthalpy of HeII at 1.15bar coming from HEPAK and corrected value of the HeII mas in the HB to describe the temperature dynamics of the HB.

The value of the enthalpy of superfluid HeII is a highly nonlinear function of temperature, see Fig. 2.5.

In the model I use enthalpy values obtained by spline interpolation of discrete values of the helium enthalpy @1.15bar coming from HEPAK.

The interpolation is performed by a EcosimPro4 function *splineInterp1D()*.

2.6 Corrected mass of HeII in the HB

Base on the observations presented above, I assumed that all internal energy of the HB is accumulated in the superfluid helium and I use the function T=f(H) of the HeII to describe the temperature of whole HB including massive iron magnet components.

In effect the mass of the HB m_H must be reduced to the mass of the superfluid helium present in the HB $m_{He,H}$ incremented by the mass of the magnet components weighted by their specific heat $\Delta m_{He,H}$:

$$m_H = m_{l,H} + \Delta m_{l,H} \tag{2.7}$$

I do not know neither the exact value of the mass of the superfluid helium inside the FP nor the specific heat of the cold magnet components.

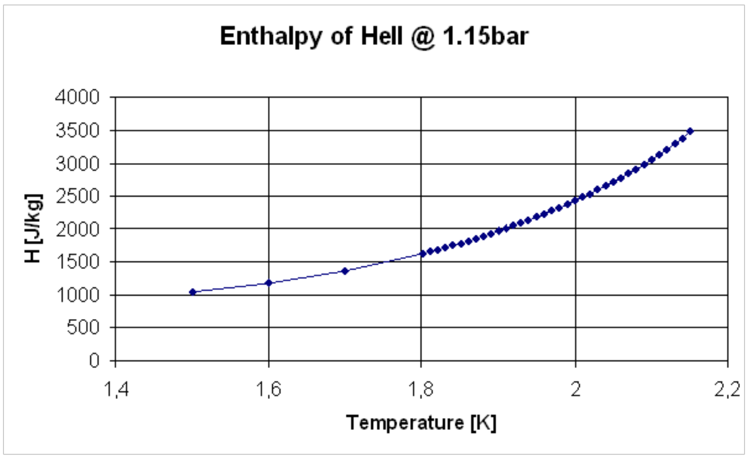

Figure 2.5: Enthalpy of HeII @ 1.15 bar.
(Source: HEPAK)

Thats is why I fitted the value by hand, starting from the value of the mass of superfluid helium that has been measured to be equal about 320 kg.

I found the corrected value, see section 3.5.2

$$m_H = 450[kg]$$

close to the value of 320 kg of the superfluid helium in the HB,that justified the approximation that the whole energy is accumulated in the HeII.

2.7 Heat transfers in the HB

Values of heat transfers in the HB $\sum Q_i(t)$ must be found in order to solve the equation 2.3.

The simplification that the HB is one-dimensional, see section 2.4.1, implicate that all inner heat transfers in the HB and heat transfer through the the cell interconnections are longitudinal and all other heat transfers into and from the HB are transversal.

The heat transfers, illustrated in the figure 2.6, are:

- static heat loads into the HB $Q_{s,i}$ that originate at ambient temperature
- dynamic heat loads into the HB $Q_{d,i}$ originating at magnet componets
- heat exchanged between the HB and BHX that cools the HB $Q_{H2B,i}$
- heat flowing from the FP into the HB, responsible for the asymmetric inverse dynamic response of the cooling loop $Q_{F2H,i}$
- longitudinal heat flow through the HB due to its non uniform temperature at the interface of two HB sectors $Q_{l,i+1/2}$
- heat exchanged through interconnections at the extremities of the HB $Q_{I,l}$, $Q_{I,r}$ for left and right interconnection respectively

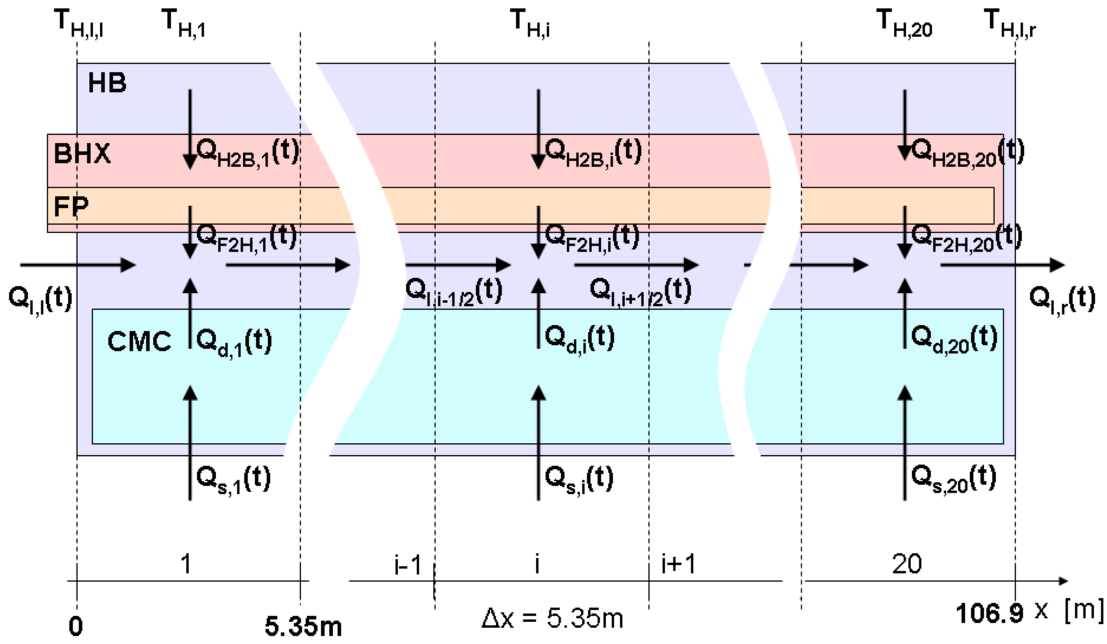

Figure 2.6: Heat transfers in the discretized HB

thus

$$\sum Q_i(t) = \begin{array}{l} Q_{I,l} - Q_{l,1+1/2} + Q_{s,1} + Q_{d,1} - Q_{H2B,1} + Q_{F2H,1}; i = 1 \\ Q_{int,i-1} - Q_{int,i} + Q_{s,i} + Q_{d,i} - Q_{H2B,i} + Q_{F2H,i}; i \in < 2 : 19 > \\ Q_{int,19+1/2} - Q_{I,r} + Q_{s,20} + Q_{d,20} - Q_{H2B,20} + Q_{F2H,20}; i = 20 \end{array} \tag{2.8}$$

2.7.1 Longitudinal Heat Transfer in the bath of HeII

The enormous heat conductivity at moderate heat flux of superfluid helium, peaking at 1.9 K, is more than million times larger [14] than this of liquid helium and makes possible longitudinal transfer of heat at small temperature differences.

This value is so large because the mechanism of heat conduction in superfluid is different than usually observed.

Mechanism of heat transfer in superfluid

The mechanism is introduced base on the article of L. Bottura and C. Rosso [14].

The two-fluid model [15] assumes that superfluid helium consists of two interpenetrating fluid components, a normal fluid and a superfluid. The superfluid component has zero entropy and no viscosity, while the viscous normal component has viscosity and carries the entropy of the mixture.

The concentration of the two components depends on temperature. Above T_λ (see section 1.3.1), the superfluid concentration is zero, but it increases as the temperature is lowered below T_λ, replacing gradually the normal component.

Local heating of stagnant superfluid helium causes a change in the relative concentrations of the superfluid and normal components. To maintain mass equilibrium and zero momentum, a flow of the superconducting component towards the heat source, and of the normal component away from the heat source must be established. Because the superfluid component has zero entropy it does not transport heat. On the other hand, the motion of the normal fluid component is associated with heat flow.

This heat transport mechanism resembles mass convection in a normal fluid, but it is not associated with a mass flow of the helium mixture. It is often referred to as counterflow heat exchange, and is responsible for the exceedingly high heat transport capability of superfluid stagnant helium. To highlight typical orders of magnitude, a temperature gradient of 0.1 Km^{-1} would result in a conduction heat flux of 2 mWm^{-2} in normal helium at 4.2 K (above T_λ), while the counterflow heat flux under the same temperature gradient would be 30 kWm^{-2} in superfluid helium at 1.8 K (below T_λ). [14]

Heat transfer in superfluid helium is hence largely dominated by counterflow heat exchange, in turn governed by the hydrodynamics of the motions of the normal and superfluid components.

In large channels with diameter in excess of 100 μm the interaction between the two components causes the generation of internal turbulence, that cause a drag between superfluid and normal fluid. This interaction, also known as the GorterMellink mutual friction mechanism [16].

In the one-dimensional case like for the HB, can be shown that the GorterMellink mutual friction term in the momentum balance for the superfluid component gives origin to a strong non-linear pseudo-conduction term in the energy transport equation [15].

Using the pseudo conduction therm, called Superfluid Thermal Conductivity Function $F(T,p)$, the heat flux q in the superfluid can be related to the temperature gradient $\frac{\partial T}{\partial x}$:

$$q^n = -F(T,p)\frac{\partial T}{\partial x} \tag{2.9}$$

The values of the Superfluid Thermal Conductivity Function $F(T,p)$ and the exponent n has been found experimentally.

Longitudinal counterflow heat transfer in a HB sector

The longitudinal counterflow heat flux introduces strong nonlinearities into the Superfluid Helium Cryogenic Circuit.

The longitudinal heat transfer between the i th and i+1 th HB sector $Q_{int,i,i+1}$, governed by the counter-flow mechanism presented in the previous section, can be calculated as:

$$Q_{l,i+1/2} = -A_{H,eff}\left(F(T_{H,i})\frac{dT_{H,i+1/2}}{dx}\right)^{\frac{1}{3}} \tag{2.10}$$

In this equation the effective cross-section area of the helium bath $A_{H,eff}$ is an experimentally fitted coefficient, see 3.5.4,

$$A_{H,eff} = 0.009[m^2]$$

that represents the part of the HB cross-section area that contributes to the longitudinal counterflow heat transfer, that means the total cross-section of longitudinal canals of superfluid helium in the HB.

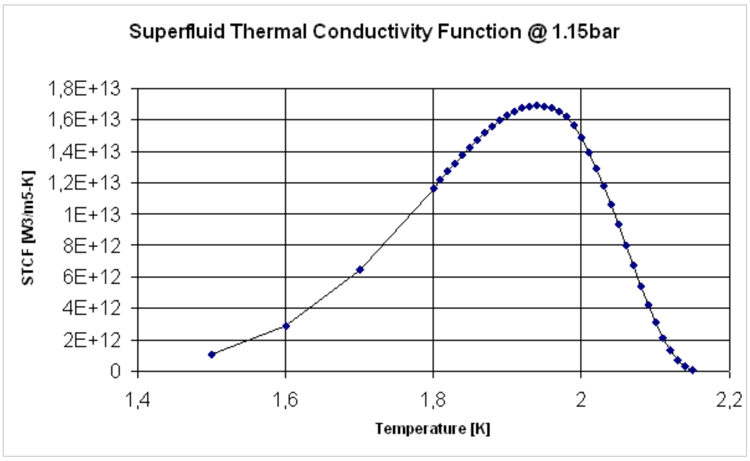

Figure 2.7: Superfluid Thermal Conductivity Function of HeII @ 1.15bar.
Source: HEPAK

The exponent 1/3 is the value of n in equation 2.9 that has been empirically determined as right for temperatures around 1.9K.

Then, the effective conductivity function F(T, p) is a property that has been tabulated from experimental data. The pressure of the helium bath p_{HB} is assumed to be constant equal 1.15 bar and the values of the function F(T) @ 1.15 bar has been taken from HEPAK, see figure 2.7

Finally, the temperature gradient in the discretized HB $\frac{dT_{H,i+1/2}}{dx}$ has been already calculated, see equation 2.6.

The longitudinal counterflow heat flux in HB sector is a highly nonlinear therm, because of the presence of the exponent 1/3 in the equation 2.11 and nonlinear temperature dependence of the effective conductivity function F(T).

Numerical optimization

Between the $Q_{l,i+1/2}$ and $\frac{dT_{H,i+1/2}}{dx}$ exist a stiff bidirectional relation as temperature of the HB sector if a function of heat flows. This causes instabilities in the numerical integration of the simulation when $\frac{dT_{H,i+1/2}}{dx} \to 0$

For this reason a modified expression for the $Q_{l,i+1/2}$ is used in the model:

$$Q_{l,i+1/2} = \begin{matrix} -A_H \left(F(T_{H,i}) \frac{dT_{H,i+1/2}}{dx} \right)^{\frac{1}{3}}; \frac{dT_{H,i+1/2}}{dx} > 1e-7K/m \\ -A_H const. \frac{dT_{H,i+1/2}}{dx} \left(F(T_{H,i}, p_H) \right)^{\frac{1}{3}}; \frac{dT_{H,i+1/2}}{dx} < 1e-7K/m \end{matrix} \tag{2.11}$$

This modification has limited the maximum derivative of the $Q_{l,i+1/2}$ as function of the $\frac{T_{H,i+1/2}}{dx}$, being also the value of the constant present in the equation, to 46415.9 at $\frac{T_{H,i+1/2}}{dx} = 1e-7$ introducing an error to calculation of the $Q_{l,i+1/2}$ for the values of $Q_{l,i+1/2} < 1J/s$

2.7.2 Heat transfer through the interconnections

Heat transfer through the interconnections is calculated in the same way like the longitudinal counterflow heat transfer in a HB sector, see the subsection above.

Source of heat load	50-75 K [W]	4.6-20 K [W]	1.9 K LHe [W]
Magnet support posts	157	9.78	1.07
Thermal shield	301.3	-	-
Radiative insulation	-	0.854	11.3
Beam Screen	-	-	1.618
Instrumentation feedthrough system (IFS)	-	-	4.254
Beam vacuum feedthrough	2.40	-	0.420
Dipole corrector feedthrough (DCF)	10.4	2.44	0.534
Beam position monitor (BPM)	-	0.928	0.604
Service Module QQS	-	0.013	0.210
Longitudinal Vacuum Barrier VB	11.6	0.029	0.424
TOTAL	**482**	**14.0**	**20.4**

Figure 2.8: Standard 107 m arc cell heat loads at the 3 cryostat temperature levels. (Source [17])

2.7.3 Static heat loads

Static Heat Loads into the HB originate at ambient temperature. Heat leaks into the HB via each Standard Cell components, see calculations presented in the "1.9 K LHe" column in the figure 2.8. The elements contributing to the static heat load are approximately equal distributed over the length of a Standard Cell.

The total heat in-leak into the HB $Q_{s,tot}$ calculated to be equal $20.4[W]$ [17] was measured to be close to 24.4 W +/- 1.6 W [18] and significantly varying in time. This means that the total static heat load into the HB must be considered as input value of the model and an observer should be developed in order estimate its actual value.

The static head load is assumed to be equal distributed over the whole length of the Standard Cell thus the static heat load into a discretized segment of the superfluid circuit:

$$Q_{s,i} = Q_{s,tot} \frac{\Delta x}{l_H} \tag{2.12}$$

where l_H stands for the HB length:

$$l_H = 106.9[m]$$

2.7.4 Dynamic heat loads

Dynamic heat loads originate at the cold magnet components due to energy dissipation. The dynamic heat load into the HB at the nominal operation conditions of the LHC machine has been calculated to be equal $17.6[W]$ [19].

The value of the dynamic heat load vary strongly in time depending on operation conditions of the LHC machine. This correlation can be used to predict its value in order to apply feed-forward control, thus dynamic heat load can be considered as input variable of the model.

2.7.5 Heat transfer to the Bayonet Heat Exchanger

The heat generated and leaking into magnet cold mass is transported by conduction across the static HB to the 107m long Bayonet Heat Exchanger (BHX) tube running all along the Standard Cell. Inside the tube, a flow of saturated helium II absorbs the heat by its vaporization in order keep the HB temperature constant, see figures 1.7, 1.8, 1.9 and 1.5.

The amount of heat extracted from a i-th sector of the HB via the BHX $Q_{H2B,i}$ is limited by the transversal thermal conductance of the thermal connection between the HB sector and the BHX $C_{th,H2B,i}$:

$$Q_{H2B,i} = (T_{H,i} - T_{B,i})C_{th,H2B,i} \tag{2.13}$$

Kapitza conductance

The transversal thermal resistance of the interconnection between the HB sector and the BHX

$$R_{th,H2B,i} = \frac{1}{C_{th,H2B,i}} \tag{2.14}$$

is a sum of the thermal resistances of 2 liquid-solid interfaces, known as Kapitza resistance, and bulk thermal resistance of BHX wall.

It has been experimentally proved that the Kapitza resistance at the interface between superfluid helium and the copper wall of the BHX dominates the transversal thermal resistance $R_{th,H2B,i}$ [20] thus the bulk thermal resistance term can be neglected.

The value of the Kapitza conductance C_{th} is a nonlinear function of temperature $\sim T^3$:

$$C_{th} = C_K A T^3 \tag{2.15}$$

where C_K is the Kapitza coefficient characterizing the interface and A stands for the interface area.

The Kapitza resistances of the pressurized helium in the HB - BHX coper wall interface is much smaller then the Kapitza resistance of the interconnection of BHX wall and saturated helium in the BHX because the pressurized helium surrounds whole BHX exterior tube perimeter and the interior wetter perimeter of the BHX is less or equal 30% of the tube perimeter. Additionally pressurized helium in the HB is warmer than the the saturated helium in the BHX. That is why I have neglected the Kapitza resistance of the pressurized helium in the HB - BHX coper wall interface.

After this simplifications the heat transfer between the i-th sector of the HB and the BHX

$$Q_{H2B,i} = (T_{H,i} - T_B)C_K A_{B,wett} T_{B,i}^3 \tag{2.16}$$

The value of the Kapitza coefficient for the coper BHX walls was measured to be in range of 920-1200 W/K4m2. [20]

The value of

$$C_K = 1200 W/K4m2$$

is used in the model.

The area of the interface between saturated HeII and coper wall of the BHX $A_{B,wett}$ is equal to the surface of the BHX tube wetted by the helium at the position corresponding to this of the HB sector.

Wetted surface area of the BHX

The investigation of the II-phase helium flow in the BHX showed that the saturated HeII would mostly operate in the stratified-flow regime [21] thus the wetted area of a BHX sector can by exactly calculated from the mass of helium present in the BHX sector.

The wetted area in the BHX is given by:

$$A_{B,wett} = P_{B,wett}\Delta x \tag{2.17}$$

where the wetted inner perimeter of the HB $P_{B,wett}$, see figure 2.9

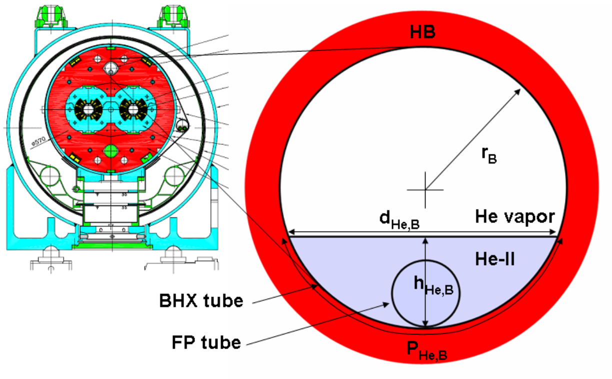

Figure 2.9: Wetted perimeter of the BHX tube.

$$P_{B,wett} = 2r_B \arccos\left(\frac{r_B - h_{l,B}}{r_B}\right) \tag{2.18}$$

where r_B is the inner radius of the BHX [19]

$$r_B = 54mm$$

and $h_{l,B}$ is the level of the saturated HeII in the BHX and is correlated with the its mass:

$$\frac{h_{l,B}}{dt} = \frac{1}{d_{l,B}} \frac{m_{l,B}}{dt} \frac{1}{\Delta x \rho_l} \tag{2.19}$$

where $d_{He,B}$ is the chord of the BHX cross-section marked by the free surface of the superfluid helium, the presence of the FP at the bottom of the BHX has to be taken into account, so that

$$d_{l,B} = \begin{array}{l} 2\sqrt{(2r_B h_{l,B} - h_{l,B}^2}; h_{l,B} > 2r_F \\ 2\sqrt{2r_B h_{l,B} - h_{l,B}^2} - 2\sqrt{2r_F h_{l,B} - h_{l,B}^2}; h_{l,B} < 2r_F \end{array} \tag{2.20}$$

The temperature and mass distribution of saturated helium in the BHX have to be found in order to calculate the heat transfer between HB and BHX.

2.7.6 Heat transfer from the Feeding Pipe

The Feeding Pipe (FP) is a small diameter pipe inside the BHX feeding saturated helium into the opposite and of the BHX. It has a common surface with the BHX and thus with the HB.

There helium flowing into the FP directly from the Joule-Thompson valve has higher temperature than the HB. That is the reason for the heat flow from the helium in FP through its wall, wall of the BHX into the HB. This heat transfer causes the asymmetric inverse change of the HB temperature in answer to the Joule-Thompson valve manipulation.

Analogically like un the case of the BHX, the heat transfer from the FP into the HB is restricted by thermal resistance of the assembly of 2 walls and 2 solid-liquid interfaces. The main difference to the BHX is that the FP has much smaller diameter than the BHX and should be full of helium for most helium flow velocities and an assumption can be made that the whole inner perimeter of the FP is always wetted.

That means heat resistance between FP and HB is dominated by a small area of common surface of the two tubes.

I have not found any description of this heat transfer in the literature. I have modeled this mechanism base on thermal diffusion law, where the heat flux is proportional to the temperature gradient. I use the temperature difference between the HB and FP $T_F - T_{H,i}$ and a coefficient C_{F2H} that has been hand fitted, see section 3.5.5. The coefficient represents the wall thickness and conductivity coefficient, and contact surface between the tubes.

$$Q_{F2H,i} = (T_F - T_{H,i})C_{F2H}\Delta x \tag{2.21}$$

The temperature of helium in the FP T_F has to be calculated in order to solve the equation.

2.8 Temperature of HeII in the BHX

Value of the saturated HeII temperature in the BHX must be found in order to solve the equation 2.16.

To simplify the model the internal longitudinal heat flows in the saturated helium has been neglected. The reason for this is that the temperature of saturated helium along the BHX is quasi uniform: it cannot take values above the saturation temperature, and this temperature, determined by the helium vapor pressure in side the BHX, is very low equal about 1.8K.

This assumption of absence of longitudinal heat flows in the saturated HeII, together with the permanent presence of the heat transfer from the HB into the BHX, that heats the superfluid helium up to the highest achievable temperature: the saturation temperature, lead to conclusion that the temperature of the HeII in the is always equal to its saturation temperature that is a function of helium vapor pressure in the BHX:

$$T_{He,B} = T_{He,B,Sat} = f(p_{HeV,B}) \tag{2.22}$$

2.8.1 Saturation temperature of HeII

The saturation temperature is a function of pressure and this relation is very well defined because is used to calibration of thermometers at very low temperatures. In the model a 8-th order polynomial approximation of this function provided by ITS-90 is used. [22].

The vapor pressure in the BHX has to be found in order to calculate the saturation temperature.

2.9 Helium vapor pressure in the BHX

The helium vapor pressure in the BHX is keeped very low because the helium vapor is pumped out from the BHX into the very low pressure Header B, see section 1.3.3 where the operational principle of the cooling loop is described.

The BHX is connected to the Header B via the overflow pot (OP), the Subcooling Heat Exchanger (SHX) and piping, thus the vapor pressure at the left end of the BHX is equal to the pressure in the Header B incremented with vapor pressure drops in the pipes, the OP and the SHX, see figure 2.10.

The pressure drops over OP and the tubes interconnecting the circuit elements have been neglected because these components have big cross-section to length factors.

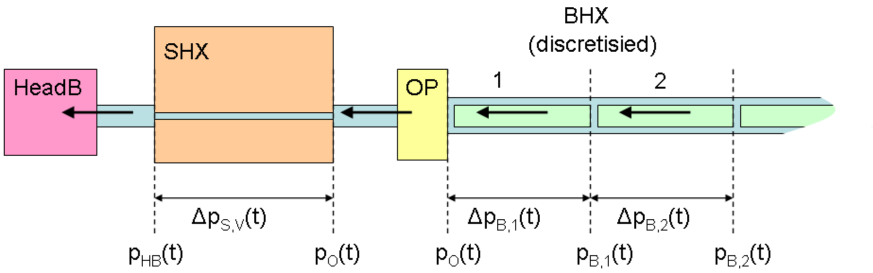

Figure 2.10: Vapor pressure drops in the cooling loop.

After this assumptions the vapor pressure at the left extremity of the BHX is equal to the pressure in the OP $p_{HeV,OP}$

$$p_O = p_{HB} + \Delta p_{S,V} \tag{2.23}$$

The calculation of the pressure drop in the Very Low Pressure (VLP) channel of the Subcooling Heat Exchanger (SHX) $\Delta p_{S,V}$ is presented in the next subsection. The pressure in the Header B p_{HB} is an input variable of the model.

Along the BHX the vapor pressure increase with the distance from the left extremity. This pressure drop in the BHX is related to the friction factor of the BHX tube and flow of vapor in the tube.

The dynamics of the vapor is very fast due to its small density and that is why it is neglected regarding the very slow dynamics of the HB temperature.

In a steady-state the pressure drop of turbulent flow of a fluid in a tube can be calculated as [21]

$$\Delta p = \psi \frac{F^2}{2\rho A^2 2r} \Delta x \tag{2.24}$$

where ψ is a friction coefficient, F mass flow, ρ density of the fluid, A and r are cross-section area and radius of the tube.

2.9.1 Pressure drop in the VLP channel of the SHX

The pressure drop in the Very Low Pressure (VLP) channel of the Subcooling Heat Exchanger (SHX)

$$\Delta p_{S,V} = c_{\psi,S,V} . F_{S,V}^2 \tag{2.25}$$

where the constant has been calculated, see section 3.5.5

$$c_{\psi,S,V} = 0.2$$

and the $F_{S,V}$ is the vapor mass through the VLP channel of the SHX, equal to the vapor mass flow leaving the BHX

$$F_{S,V} = F_{HeV,B,1/2} \tag{2.26}$$

2.9.2 Discretization of the BHX

The vapor flowing through the BHX is a sum of vapor entering the BHX from the FP and the vapor created in the BHX as the effect of the vaporization of the saturated helium.

The vaporization mass flow in the BHX is proportional to the heat flowing into the BHX from the HB, that depends on the temperature of the HB, that is a value distributed over the HB length, thus the vaporization mass flow in the BHX is also a distributed value. That is one of the reasons for the discretization of the BHX.

I have discretized the BHX in the same way as the HB: the BHX tube has been subdivided into 20 sectors each 5.35m long, see figure 2.12.

2.9.3 Enthalpy of vaporization of the helium and vaporization rate in a BHX sector

The mass flow of vapor created by evaporating helium in a BHX sector $F_{l2v,B,i}$,see Fig. 2.12, is easy to find:

$$F_{l2v,B,i} = \frac{Q_{H2B,i}}{\Delta_V H_{He}} \tag{2.27}$$

This expression is true at the assumption made before that helium is always at saturation temperature - there is no heat needed to warm up the helium to the saturation temperature thus the heat input is entirely used for the vaporization of liquid helium.

The value of the enthalpy of vaporization of the helium

$$\Delta_V H_{He} = 23.4\frac{J}{g}$$

is quasi constant, independent of temperature and pressure, and has been calculated as a difference of the values of enthalpy of superfluid and vapor helium at saturation at 16 mbar (data from HEPAK): $H_l(@1.793K) = 822\frac{J}{kg}$ and $H_v(@1.794K) = 24200\frac{J}{kg}$ thus

$$\Delta_V H_{He} = H_v - H_l = 23.4\frac{J}{g} \tag{2.28}$$

2.9.4 Helium vapor mass flow inside the BHX

As mentioned before, see equation 2.24, the pressure drop over a BHX sector $\Delta p_{B,i}$ is proportional to the mass flow of helium vapor in the BHX, that is equal to the sum of vapor mass flows entering the BHX sector from the neighbor sector, or from the FP in case of sector number 20, and the vapor created in the BHX as an effect of vaporization of the saturated helium.

The rate of helium evaporation is assumed to be equal distributed along the sector. **The vapor flows in the BHX in the negative x direction**, thus the mass flow along the BHX sector $F(x)$, see figure 2.11

$$F_{v,B,i}(x) = -F_{v,B,i+1/2} + \frac{F_{l2v,B,i}}{\Delta x}(x - x_{i+1/2}) \tag{2.29}$$

where the mass flow between the i-th and $i+1$-th sector, illustrated in the figure 2.12):

$$-F_{v,i+1/2} = \begin{matrix} F_{v,F2B}; i = 20 \\ F_{v,i+3/2} + F_{l2v,B,i+1}; i \in < 1:19 > \end{matrix} \tag{2.30}$$

where the value of the mass flow of vapor helium from the FP into $F_{v,F2B}$ must be found.

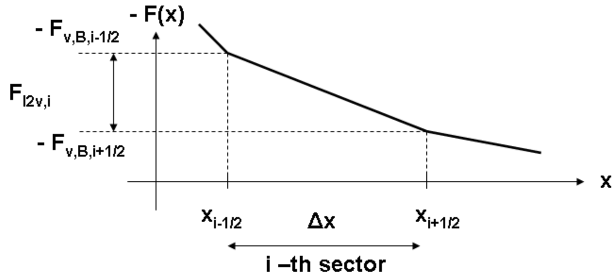

Figure 2.11: Vapor mass flow inside a BHX sector.

2.9.5 Helium vapor pressure in a BHX sector

Helium vapor pressure in a BHX sector is equal to sum of the pressure in the OP p_O and all pressure drops in the BHX sectors between the sector and the OP:

$$p_{B,i} = p_O + \sum_{j=1}^{i} \Delta p_{B,j} \tag{2.31}$$

The pressure drop in a BHX sector has been found after integration of the equation 2.24 over the sector length Δx with the mass flow distribution along the BHX sector $F(x)$ presented above:

$$\Delta p_B = \psi_B \frac{F^2_{v,B,i+1/2} - F_{v,B,i+1/2}\left(\frac{F_{l2v,B,i}}{\Delta x}\right) + \frac{1}{3}\left(\frac{F_{l2v,B,i}}{\Delta x}\right)^2}{2\rho_{v,B} A_B^2 2 r_B} \Delta x \tag{2.32}$$

where r_B and A_B are the inner radius and cross-section area of the BHX [19]

$$r_B = 54mm$$
$$A_B = \pi r_B^2$$

The friction coefficient of the tube [19]

$$\psi_B = 0.02$$

Since the void fraction in the BHX tube is large a simplification is made that the cross-section for the helium vapor flow is always equal to the cross-section of the tube A_B.

To simplify the computation, the vapor density $\rho_{v,B}$ is assumed to be constant along the BHX corresponding to the value of pressure at the OP

$$\rho_{v,B} = \rho_v @ p_O \tag{2.33}$$

This is justified by the fact that the pressure drop along whole length of the BHX, takes value around 0.2mbar and the nominal value of pressure in the BHX is equal 16mbar what gives only $\frac{0.2mbar}{16mbar} = 1.2\%$ of relative pressure change along the BHX.

The calculation of vapor mass flowing from the FP to the BHX initiating the vapor flow through the BHX is presented in the section 2.14.

2.10 HeII mass distribution in the BHX

The mass distribution of the saturated HeII in the BHX must be found in order to calculate the heat transfer between the HB and the BHX, see section 2.7.5.

The modeling of the superfluid helium mass distribution in the BHX is a difficult problem.

One reason for this are the unusual physical properties of the superfluid helium, another fact is that the superfluid is flowing along the BHX, and its dynamics must be modeled what significantly increase the computational complexity of the problem.

2.10.1 CFD - Computational Fluid Dynamics

The numerical modeling of fluid dynamics is the center of interest of Computational Fluid Dynamics.

The classic CFD methods base on discretization and numerical solution of the Navier-Stroke equations describing the fluid dynamics. This is a set of partial differential equations (PDE) describing mass, momentum and energy conservation in a fluid enhanced with boundary conditions. This methodology gives very good results but needs small discretization intervals in space and time, thus is very slow.

I found experimentally that the simulation of saturated HeII dynamics runs fast enough to be considered as applicable in the NMPC only when the BHX is discretized in less than 20 sectors and the maximal integration interval, corresponding to the time discretization, takes values bigger than 10s. That indicates spatial discretization interval is equal 5.35m, and the temporal discretization interval equal 10 s.

Classical methods mentioned above need much smaller discretization intervals to compute fluid flow at average velocity about 0.15 m/s - that is the measured velocity of superfluid flow in the BHX [23].

2.10.2 Simplified method of the modeling of HeII mass distribution

I have developed a simplified approach to the problem base on the Finite Volume method in order to enable a fast simulation of the model. The BHX is divided into 20 volumes where we can consider that the variables are homogenous as showed in the figure 2.12. Moreover two spaces for superfluid and vapor helium are considered in each volume.

This approach is very simple and should be refined in the future in order to improve the precision of the model.

The main simplification made is the assumption that the superfluid helium dynamic behavior corresponds to an incompressible liquid.

Mass conservation

The important property of the method is mass conservation of the fluid in each finite volume sector. This property assures that no HeII will be "lost" in the BHX.

The mass conservation equation for the constant volume of the i-th sector, illustrated in the Fig. 2.12):

$$\frac{dm_{l,B}}{dt} = F_{l,B,i-1/2} - F_{l,B,i+1/2} - F_{l2v,B,i} \tag{2.34}$$

with the boundary condition

$$F_{l,B,20+1/2} = F_{l,F2B} \tag{2.35}$$

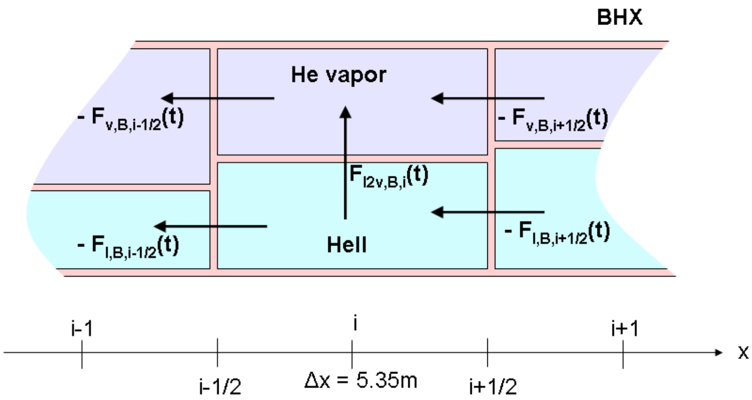

Figure 2.12: Discretization of the BHX.

The evaporation mass flow $F_{l2v,B,i}$ from this equation has been already calculated, see section 2.9.3.

The longitudinal mass transfer between BHX sectors $F_{l,B,i+1/2}$ is always negative because the superfluid helium in the BHX flows in the negative x-direction.

$$F_{l,B,i+1/2} = u_{l,B,i+1/2} A_{B,wett,i} \rho_l \tag{2.36}$$

$A_{B,wett,i}$ and ρ_l were already calculated, see sections 2.7.5 and 2.6 respectively.

Implementation of spatial distribution

Calculation of the velocity of HeII flow at the interface of two BHX sectors $u_{l,B,i+1/2}$ implements element of delay introduced by spatial distribution of the BHX:

$$\frac{du_{l,B,i+1/2}}{dt} = \left(u_{l,B,i+1} - u_{l,B,i+1/2}\right) \frac{1}{\Delta x} \tag{2.37}$$

Where $u_{l,B,i+1}$ is the velocity of HeII flow in the center of the upstream neighbor sector.

Momentum conservation

The momentum conservation principle for a fluid mass present in the BHX sector:

$$\frac{dm}{dt}u + \frac{du}{dt}m = \sum F \tag{2.38}$$

where F are the forces acting on the mass, m is the mass of the fluid and u its velocity.

In order to find the HeII flow velocity inside the BHX sector $u_{l,B,i}$, the equation is approximated by taking into account the change of average value of the velocity in a BHX sector, caused by mass flows into and from the sector:

$$\frac{du_{l,B,i}}{dt} = \frac{F_{l,B,i+1/2} u_{l,B,i+1/2}}{m_{l,B,i}} + a_{l,B,i} \tag{2.39}$$

where $m_{l,B,i}$ stands for mass of HeII present in the i-th BHX sector and $a_{l,B}$ is an acceleration term.

The acceleration term represents all forces acting on the flowing fluid mass: pressure gradients and viscous forces in the superfluid and at the BHX walls:

$$a_{l,B} = \frac{dh_{l,B,i}}{dx}G - \frac{dp_{v,B,i}}{dx}\frac{1}{\rho_l} - u_{l,B,i}abs(u_{l,B,i})\psi_{l,B}\frac{P_{B,wett,i}}{A_{B,wett,i}} \tag{2.40}$$

I have not implemented the translation derivative translating the forces acting in the moving frame of liquid into the static reference frame for sake of simulation stability. This should not introduce a considerable error because the velocity of the flow and gradients are small.

In the equation, the HeII level gradient $\frac{dh_{l,B,i}}{dx}$ is calculated using central finite differences approach

$$\frac{dh_{l,B,i}}{dx} = \begin{array}{l} \frac{h_{l,B,i+1}-h_{l,B,i-1}}{2\Delta x}; i \in < 2; 19 > \\ \frac{-3h_{l,B,1}+4h_{l,B,2}-h_{l,B,3}}{2\Delta x}; i = 1 \\ \frac{3h_{l,B,20}-4h_{l,B,19}+h_{l,B,18}}{2\Delta x}; i = 20 \end{array} \tag{2.41}$$

G is the gravity constant

$$G = 9.81[m/s2]$$

the gradient of the vapor pressure

$$\frac{dp_{v,B,i}}{dx} = \frac{p_{v,B,i+1/2} - p_{v,B,i-1/2}}{\Delta x} \tag{2.42}$$

The friction pressure loss has been approximated using a value of the pseudo-friction factor for the HeII flow in the BHX $c_{\psi,l,B}$ weighted by the ratio of the wetted BHX tube perimeter to cross-section area $\frac{P_{B,wett,i}}{A_{B,wett,i}}$. These variables has been calculated in previous section.

The pseudo-friction factor has been hand fitted, see section 3.5.6

$$c_{\psi,l,B} = 0.0002$$

Boundary conditions

The boundary conditions for the HeII flow in the BHX are the velocity and mass flow of the saturated helium flowing into the BHX from the FP

$$u_{l,B,20+1/2} = u_{l,F2B}$$

$$F_{l,B,20+1/2} = F_{l,F2B}$$

2.11 Helium flow in the Feeding Pipe (FP)

The mass flow and velocity of helium in the Feeding Pipe (FP) must be found in order to define the boundary conditions for the helium flows in the BHX: the superfluid flow, see previous section, and the vapor flow, see section 2.9.4.

The effect of vapor condensation inside the FP caused by the heat flowing from the FP to the HB is neglected.

2.11.1 He Mass flow in the Feeding Pipe (FP)

The modeling of the mass flow inside the FP must be simplified as much as possible in order to enable fast simulation of the model.

Supercritical liquid helium and a small fraction of vapor, created during expansion of the helium in the JT valve, flows into the FP from the JT valve.

FP has a small inner diameter [19]

$$r_{F,in} = 5[mm]$$

that is why an assumption can be made, that the FP is always full of helium.

FP is a 106.9 m long component. For simplification sake, the dynamics modeling of the two-phase helium flow inside the FP has been modelled in a very simplified way, and the vapor and liquid velocities are assumed to be equal.

Mass flows of helium liquid and vapor entering the FP $F_{l,F,1/2}$ and $F_{v,F,1/2}$ are equal to the mass flows of helium liquid and vapor leaving the JT valve $F_{l,d,J}$ and $F_{v,d,J}$

$$F_{l,F,1/2}(t) = F_{l,J} \tag{2.43}$$

$$F_{v,F,1/2}(t) = F_{v,J} \tag{2.44}$$

I have assumed that the FP is full of helium and the flow changes propagate relatively fast over the 106.9 m long FP. I have modeled the mass flow leaving the FP:

$$\frac{dF_{l,F,20+1/2}}{dt} = (F_{l,F,1/2} - F_{l,F,20+1/2})\frac{1}{c_{inert,l,F}} \tag{2.45}$$

where the $c_{inert,l,F}$ is a coefficient representing the inertia of the liquid helium present in the FP.

Its value has been hand fitted, see section .

The dynamics of the helium vapor in the FP has been neglected

$$F_{v,F,20+1/2}(t) = F_{v,F,1/2} \tag{2.46}$$

2.11.2 Flow velocity in the Feeding Pipe (FP)

For simplification sake, the dynamics modeling of the two-phase helium flow inside the FP has been strong simplified, and the vapor and liquid velocities are assumed to be equal. Only the velocity of the flow leaving the FP is calculated

$$u_{lv,F,20+1/2} = \left(F_{l,F,20+1/2} + F_{v,F,20+1/2}\right)\frac{1}{A_F \rho_{lv}} \tag{2.47}$$

where A_F and $\rho_{lv,F}$ are the inner cross-section area of the FP and density of the two-phase helium respectively.

The density of the two-phase flow $\rho_{lv,F}$ has been found as

$$\rho_{lv,F} = \frac{(F_{l,F,20+1/2} + F_{v,F,20+1/2})\rho_{l,F}\rho_{v,F}}{F_{l,F,20+1/2}\rho_{v,F} + F_{v,F,20+1/2}\rho_{l,F}} \tag{2.48}$$

the He vapor density $\rho_{v,F}$ is a function of pressure but for simplification sake I fixed its value to the value measured at 25mbar

$$\rho_{v,F} = 654.4[g/m3]$$

2.12 Mass flow through Joule-Thompson Valve

The mass flows of helium liquid and vapor leaving the JT-Valve $F_{l,JT}$ and $F_{v,JT}$ must be found in order to find the mass flows of the two-phase helium in the FP.

For a simplification sake all transient states of flows in the JT valve and the FP are neglected.

2.12.1 Samson method for mass flow calculation

In a steady state the mass flow through the the JT Valve is a function of the valve lift, that is the valve opening.

From the data provided by the valve manufacturer (Linde Babcock) the valve is equal percentage type with the valve coefficient [23]

$$K_{VS} = 0.12[m3/h]$$

The relation between the valve lift $x$and the mass flow through the valve $F_{lv,J}$ for the equal percentage type valve takes form, see Samson method in [26]

$$F_{lv,J}(x) = 31.62K_{VS}R^{x-1}\sqrt{\rho_l(p_{u,J} - p_{d,J})} \tag{2.49}$$

where R is the rangeability of the valve and the difference of the valve upstream and downstream pressure $p_{u,J} - p_{d,J}$ represents the pressure drop in the valve.

2.12.2 Upstream pressure at the JT valve

The upstream end pressure is equal to the pressure of the supercritical helium in the Header C p_{HC} reduced by pressure drop in the Super Critical channel of the Subcooling Heat Exchanger $\Delta p_{S,S}$

$$p_{u,J} = p_{HC} - \Delta p_{S,S} \tag{2.50}$$

The pressure drop $\Delta p_{S,S}$ is a function of the mass flow of pressurized He through the SHX but is defined in the specification, see [24], as

$$\Delta p_{S,S} < 0.2[bar]$$

thus is neglected in the model.

In effect the upstream pressure at the JT valve is equal to the pressure in the header C, that is assumed to be constant, having design value

$$p_{u,J} = p_{HC} = 3[bar]$$

2.12.3 Downstream pressure at the JT valve

The downstream pressure at the JT valve is equal to the pressure in the BHX $p_{B,20+1/2}$ incremented by the pressure drop in the FP.

The FP is sized so that the pressure drop, varying in time as function of flow velocity inside the FP tube, is small in range of teens of mbars. [19], thus is neglected by the calculation of the mass flow through the JT valve.

2.12.4 Liquid and vapor helium mass flow leaving the JT valve

The conclusion of the investigation on up and down -wind pressures at the JT valve is that the pressure drop along the valve is quasi constant

$$p_{u,J} - p_{d,J} = 3[bar]$$

Putting this value into the equation 2.49 I have found the helium mass flow through the JT valve

$$F_{lv,J}(x) = 23.7R^{x-1} \tag{2.51}$$

and the rangeability has been found, see section 3.5.8

$$R = 68.6$$

In normal conditions, a vapor fraction is present in this flow because during the expansion of helium in the JT valve, helium pressure falls to the values smaller than the vapor pressure of helium at given temperature. This forces flash helium evaporation cooling itself down to the saturation temperature.

The vapor mass flow created in this process can be found easy as

$$F_{v,d,J} = F_{l,u,J}\Delta H_{l,J}\frac{1}{\Delta_V H_{He}} \tag{2.52}$$

where the change of liquid helium enthalpy

$$\Delta H_{l,d,J} = H_{l,u,J} - H_{l,d,J} \tag{2.53}$$

The enthalpy of vaporization of helium $\Delta_V H_{He}$ has been described in the section 2.9.3. The values of helium enthalpy are function of temperature and pressure. In the model the interpolated values of enthalpy base on discrete values as function of temperature ,coming from HEPAK are used. Precisely enthalpy values measured at 3 bar are used to interpolate the upstream value $H_{l,u,J}$ and the values measured at saturation pressure for $H_{l,d,J}$.

The downstream mass flow of liquid helium can be found as the difference between the upstream liquid helium mass flow in the JT $F_{lv,J}$ and the downstream vapor fraction

$$F_{l,d,J} = F_{lv,J} - F_{v,d,J} \tag{2.54}$$

2.13 Temperature distribution over the FP

The inner longitudinal heat flow in the helium flowing inside the FP is neglected. In this configuration the temperature of the helium in the FP depends only on the pressure inside the FP and heat interchanged with the HB.

The temperature of helium inside the HB cannot be larger then the saturation temperature of helium at given pressure.

The temperature of helium entering the FP after expansion in the JT valve is equal saturation temperature thus is determined by the pressure drop along the FP.

I have observed in my model, that the fall of helium temperature along the FP caused by the heat flow from the FP to the HB is much faster then the fall of the saturation temperature. That is why I have assumed that after the flash vaporization in the JT valve no vaporization takes place along the FP tube. The condensation of the vapor in the FP has been also neglected, for simplification sake, even if it can significantly affect the temperature distribution.

2.13.1 Discretization of the FP

The heat flow from the FP to the HB depends on both FP and HB temperatures that are distributed variables. In order to calculate these distributed values the FP is discretized in 20 segments exactly like the HB, see section 2.4.4.

2.13.2 Energy conservation

The temperature of liquid helium flowing along the FP is correlated with the energy flow related to the helium flowing inside the FP, thus the temperature can be found using energy conservation principle in simple heat exchanger configuration, assuming the constant mass flow of helium along the FP, the enthalpy of liquid helium along the FP

$$H_{l,F,i+1/2} = H_{l,F,i-1/2} - Q_{F2H,i}/F_{l,F} \tag{2.55}$$

And the temperature is function of the enthalpy and is calculated in the model by interpolation of discrete values of $H = f(T)$ from HEPAK.

$$T_{l,F,i+1/2} = f(H_{l,F,i+1/2}) \tag{2.56}$$

The values of the temperature are calculated one after another starting from the $T_{l,F,1/2}$ that is equal to saturation temperature at the end of the FP, which is a function of pressure.

2.13.3 Pressure drop along the FP

The pressure drop along the FP has to be calculated in order to find the temperature of the helium in the FP.

I assumed that the pressure drop of the two-phase flow in the FP can be calculated in the same way like the pressure drop of a single-phase flow.

The simplified expression for the pressure drop along the FP is used

$$\Delta p_F = 16.2 + c_{\psi,F} u^2_{l,F,20+1/2} \tag{2.57}$$

where the velocity of the flow at the end of the FP $u_{l,F,20+1/2}$ has been already found,, see section above, and pseudo friction factor has been hand fitted, see section 3.5.3

$$c_{\psi,F} = 20000$$

2.14 Mass flow of helium entering the BHX

I assumed that no evaporation and condensation takes place in the FP, and that the helium temperature falls along the FP only as effect of the heat transfer from the FP into the HB. In effect the helium leaving the FP can have higher temperature than the saturation temperature of helium in the BHX, causing flash evaporation of helium.

The mass flow of the vapor created in this process can be calculated analogically like for the JT valve

$$F_{l2v,F2B} = F_{l,F,20+1/2} \Delta H_{l,F2B} \frac{1}{\Delta_V H_{He}} \tag{2.58}$$

where the change of liquid helium enthalpy between the FP and BHX

$$\Delta H_{l,F2B} = H_{l,F,20+1/2} - H_{l,B,20+1/2} \tag{2.59}$$

In effect the mass flows of superfluid and vapor helium entering the BHX

$$F_{l,B,20+1/2} = F_{l,F,20+1/2} - F_{l2v,F2B} \tag{2.60}$$

$$F_{v,B,20+1/2} = F_{v,F,20+1/2} + F_{l2v,F2B} \tag{2.61}$$

Chapter 3

Model adjusting and simulation

Many model coefficients have to be fitted by hand in order to get the best agreement of simulation results with the available experimental data. The only available experimental data of Standard Cell came from the String2 Phase3 experiment, so the Standard Cell during adjusting and validation must be in the same configuration like in the experiment.

3.1 String2 Phase3 experiment

In the String2 Phase3 experiment the construction differences between the Standard Cell prototype and the series LHC Standard Cell are negligible.

The difference between the experimental and the normal LHC machine operating conditions was caused by the fact that in the experiment the extremities of the Standard Cell were not connected to other cells but to an electrical feed-box DFBX and to a magnet return box MRB, introducing additional heat flow throw the interconnections, see Fig. 3.1

The heat flow through the electrical feed-box DFBS lambda plate into the first quadropole MQ1 of the Standard Cell has been evaluated to be equal 7.2 1.1 W [25]. About 1W of heat flew into the last dipole of the Standard Cell MB6 through the interconnection to the magnet return box MRB with its extra jumper.

3.1.1 Modeling the DFBX

The DFBX has been modeled as a lumped mass of 30 kg of superfluid helium connected to the Standard cell via a 1 meter long interconnection

$$l_{D2H} = 1[m]$$

with the cross-section equal to the effective cross-section of the HB $A_{H,eff}$. This configuration lets approximate the heat flow dynamics between the Standard Cell and the DFBX. In the model

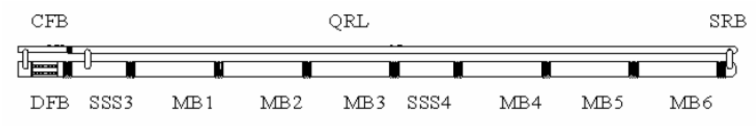

Figure 3.1: Schematic of the String2 phase3 experiment.

7.2 W of heat is continuously flowing into the lumped mass of helium. The heat transfer from the DFBX into the HB is described by the function $q_{GM}(\frac{T_{HB;IC}-T_{DFBX}}{l_{DFBX2HB}})$ implementing the Gorter-Mellink counterflow heat transfer mechanism, see section 2.7.1. Two equations describe the thermal dynamics of the DFBX, analogically tike in the case of the HB

$$\frac{dH_D}{dt} = (7.2W - Q_{D2H})\frac{1}{m_{l,D}}$$

$$\frac{dT_D}{dt} = f(H_D)$$

$$Q_{I,l} = Q_{D2H} = A_{H,eff}q_{GM}(\frac{T_{HB;IC} - T_{DFBX}}{l_{DFBX2HB}})$$

3.1.2 Modeling the MRB

The dynamics of the heat flow between the MRB and the Standard Cell in the String2 experiment is neglected. Thermal influence of the MRB is modeled as 1W of constant heat flow through the interconnection

$$Q_{I,r} = 1W$$

3.2 Estimation of the static heat load

The static heat load present during the String2 experiment has to be estimated in order to set the operational point of the simulation.

It is done in a very simple way by an observer using the model of the cryogenic circuit.

In the observer configuration the control input of the model is the static heat load, to be estimated, and the output are the magnet temperatures. The regulation error of the temperature

$$e_T = T_{m,exp} - T_{m,sim} \tag{3.1}$$

where T_e and T_m are experimental and simulated magnet temperatures. The simulated magnet temperatures are calculated as showed in the section 2.4.5.

The error is feed into the PI controller that calculates the estimated value of the static heat load $Q_{s,est}$, see fig. 3.2

$$Q_{s,est} = k_p e_T + k_i \int e_T \tag{3.2}$$

The gains has been found experimentally to be equal: integral

$$k_i = 1e3$$

and proportional

$$k_p = 1e5$$

The time evolution of the heat load estimation is presented in the figure 3.3.

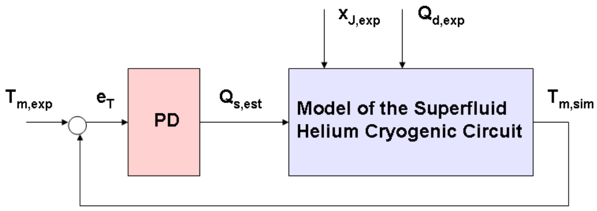

Figure 3.2: architecture of the static heat load estimator.

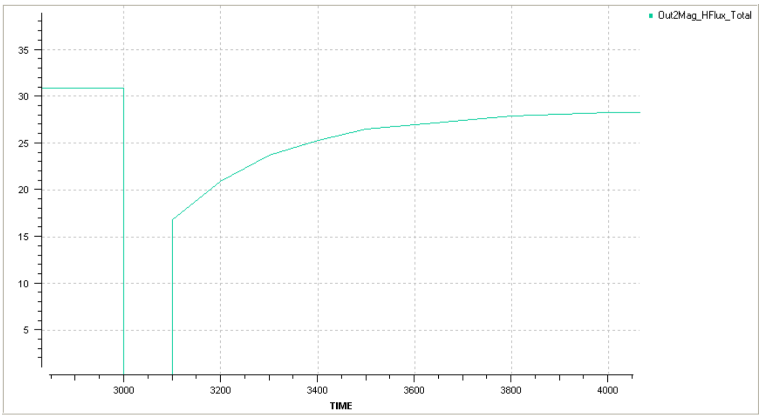

Figure 3.3: Time evolution of the heat load estimation.
The observer has been activated at T=3000.

Name	Date	phase	JT valve lift	Heat Loads
Nominal1	2002/07/09	2	pulse down and pulse up	0
Nominal3	2003/05/30	3	pulse down and pulse up	0
Hload3	2002/07/09	3	35.2%	21W@MQ2
Mixed1	2002/07/09	3	pulse down and pulse up	21W@MQ1

Table 3.1: Configuration of the String2 experiments

3.3 Experimental data

The data from the 4 String2 experiments has been used to tune and validate the model. The performed experiments are presented in the table 3.1.

Experiment "Nominal1" was performed on the prototype in the phase 2, when the static heat loads were significantly higher, and its distribution probably different, than in phase 3 or in the Standard Cell. The 3 other experiments were performed on the String2 phase3 prototype.

3.3.1 Additional heaters

In the String prototype additional heaters were installed in the HB in order to simulate the additional heat loads. Unfortunately I have not found information about exact localization of the heaters, I was told that they are close to each magnet extremities.

In the experiments used in the adjusting and validation of the model only 2 heaters are used, the heater in the first and second quadropole MQ1 and MQ2.

After simulation of the model with heats loads places on both sides of the MQ2 I have decided that heaters must have been located close to interconnections MB3-MQ2 and DFBX-MQ1.

I have modeled the additional heat as dynamic heat entering into the HB sectors that are located at position corresponding to the mentioned above:

$$Q_{d,1} = Q_{MQ1}$$

$$Q_{d,10} = \frac{1}{2} Q_{MQ2}$$

$$Q_{d,11} = \frac{1}{2} Q_{MQ2}$$

3.3.2 Experiment configuration

The configuration of the experiments is presented in the table 3.1.

All the experiments were performed at pressure in the HeaderB

$$p_{HeadB} = 16[mbar]$$

3.3.3 Measured variables

The measured variable used to validate the model are the magnet temperatures and the temperature of supercritical pressurized helium after subcooling in the SHX.

Additionally in the experiment Nominal1 the wetted length of the BHX is estimated base on the helium level measurements in the BHX.

3.3.4 Data accuracy

The accuracy of the temperature measurements is +/- 10mK.

3.4 Use of experimental value of the super critical helium temperature.

Unfortunately I have not succeed to close the cooling loop of the superfluid helium cryogenic circuit. That means that I have not found a way to calculate the value of the temperature of the super critical helium after subcooling in the SHX. That is why the experimental value of the temperature is feed into the model during the simulation.

3.5 Adjusting model parameters

The model parameters that are hand fitted have to be adjusted prior to the model validation. The parameters are:

- Specific heat capacity of magnet cold components
- Effective cross-section of the HB
- Pseudo-heat conductance coefficient of the thermal interface between the FP and HB
- Pseudo-friction coefficient of the VLP channel of the SHX
- Pseudo-friction coefficient of the BHX for the superfluid flow
- Pseudo-friction coefficient of the FP
- Inertia coefficient of the liquid helium in the FP
- Rangeability of the JT valve

3.5.1 Important remark

In the figures the thin curves represent experimental data and bold are the simulation results as default.

3.5.2 Corrected mass of the HeII in the HB

I choose the corrected mass of the HeII in the HB as the first parameter to adjust because its tuning is not sensible to the values of other coefficients.

The data from String2 "hload3" experiment was used as reference. During the experiment 21 watts additional heat were applied into the second quadropole MQ2.

First I have adjusted roughly the effective cross-section of the HB and the pressure drop in the BHX in order to get the spatial temperature distribution close to that from the experiment. I have found $A_H = 0.01[m2]$ and pressure at the end of the BHX $p_{HeVap;BHX;20} = 16.3mbar$

Then the experiment was simulated with values of the corrected mass and a value corresponding to the best agreement between simulated and experimental dynamics of the HB temperature around the MQ2 (where the heat was applied) was chosen, see Fig. 3.4:

The simulation results were closest to the experimental data for the value

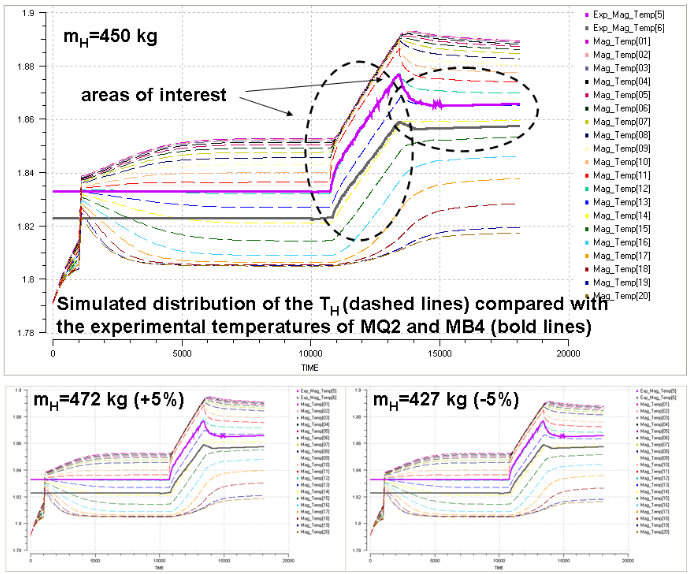

Figure 3.4: Adjusting of the corrected HB mass.

$$m_H = 450[kg]$$

As one can see in the figure 3.4 I decided to compare the experimental values of MQ2 and MB4 with simulated temperatures for all HB sectors - that let me see the whole simulated temperature distribution and not only the temperatures corresponding to the MQ2 and MB4 magnet positions. I did it that way for two reasons. First, I I haven't found information about where the heaters and the thermometers were exactly installed in the magnet and second I was not sure of other coefficients like A_{HB}, so the best way to compare the experimental data with the simulation is to observe temperature distribution around the supposed heater location.

3.5.3 FP "inverse response" parameters: C_{FP2HB} and $c_{\psi,F}$

The pseudo-heat conductance coefficient of the thermal interface between the FP and HB C_{FP2HB} together with the pseudo-friction coefficient of the FP $c_{\psi,F}$ determine the heat transfer distribution along the FP and in effect the shape of the asymmetric inverse response of magnet temperature on the JT valve manipulation.

The pseudo-heat conductance coefficient of the thermal interface between the FP and HB C_{FP2HB} determines the total value and distribution of heat flowing from the FP into the HB.

The pseudo-friction coefficient of the FP $c_{\psi,F}$ determines the pressure drop inside the FP and in effect the saturation temperature of helium at the downstream side of the JT valve thus also the temperature of helium entering the FP.

I have adjusted the pseudo-friction coefficient in order to get the value of the pressure drop along the FP like in the literature [19].

I found the initial value

$$c_{\psi,F} = 500$$

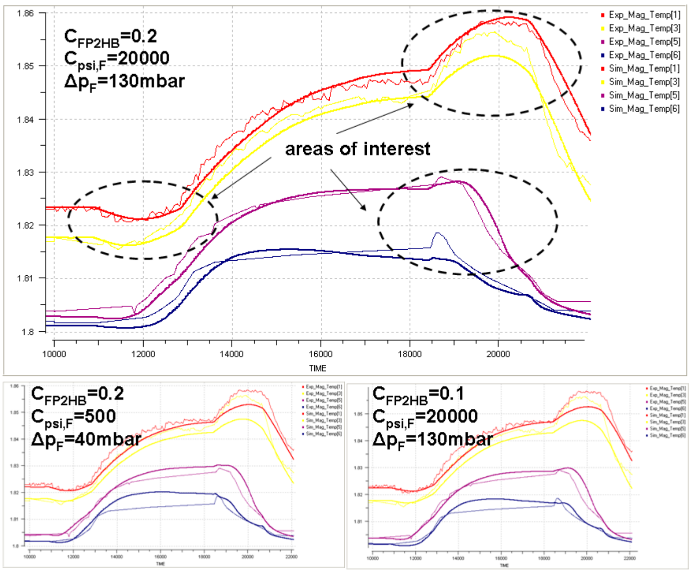

Figure 3.5: Adjusting the FP "inverse response" parameters: C_{FP2HB} and $c_{\psi,F}$.

The both coefficients were adjusted simultaneously using the experiment nominal3 base on the observation of the amplitude of the inverse response shape on the JT valve manipulation and the total result of energy flow into the HB - taking into account the values of the magnet temperatures at the end of the experiment.See Fig 3.5

I obtained the best results for

$$C_{FP2HB} = 0.2$$

and

$$c_{\psi,F} = 20000$$

The value of pseudo friction factor $c_{\psi,F} = 20000$ corresponds to much bigger pressure drop inside the FP than found in literature

$$\Delta p_F = 130mbar$$

Possibly the coefficient has been chosen badly.

3.5.4 Effective cross-section of the HB

The effective cross-section of the HB has been adjusted in a static case, without changing of heat loads or manipulating the JT valve.

As the experimental data, I have chosen the steady state values of the magnet temperatures from the "nominal3" experiment, corresponding to the first recorded values, before the manipulation of the JT valve has taken place.

I have adjusted the effective cross-section of the HB in order to get maximum similarity between the simulated distribution of the magnet temperatures along the Standard Cell and the experimental values.

The results are presented in the figure 3.6

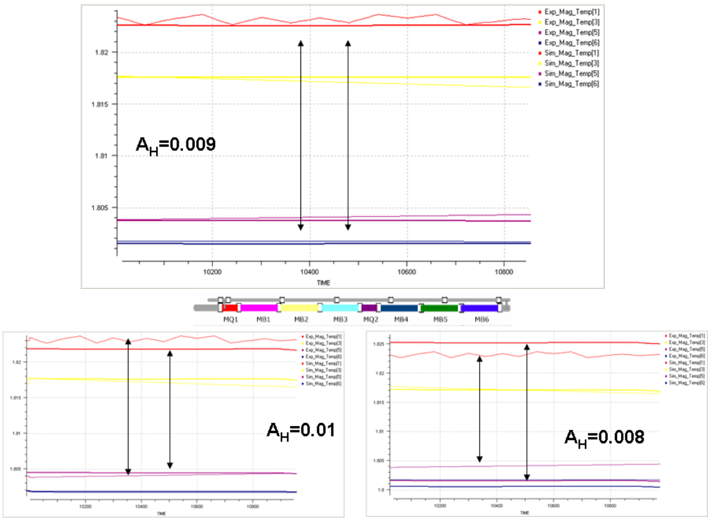

Figure 3.6: Adjusting the effective cross-section of the HB.

The simulation results are closest to the experimental data for the value

$$A_H = 0.01[m2]$$

3.5.5 Pseudo-friction coefficient of the VLP channel of the SHX

The pseudo-friction coefficient of the VLP channel of the SHX influences the pressure drop in the SHX VLP channel thus the pressure in the BHX thus the saturation temperature of helium inside the BHX, thus the minimal temperature of the magnet - the temperature of the dipole MB6 that in the case of a separate Standard Cell, like in the String2 configuration.

The coefficient has been adjusted in order to find the best agreement of the simulated temperatures of the dipole MB6 during the "nominal1" experiment. See Fig. 3.7

3.5.6 Pseudo friction coefficient for HeII flow in the BHX

The pseudo friction coefficient for HeII flow in the BHX influences very strongly the mass distribution of helium inside the BHX and the velocity of the helium flow inside the tube.

In the fist approach I tried to fit the coefficient to achieve the agreement of the simulated average speed of superfluid helium in the BHX, with the experimental value equal 0.15 [m/s]. [28]

This needed the value of the coefficient smaller than 0.0001. Unfortunately simulation with so small coefficient was very slow. I have chosen the coefficient in order to get right speed of simulation

$$c_{\psi,l,B} = 0.0002$$

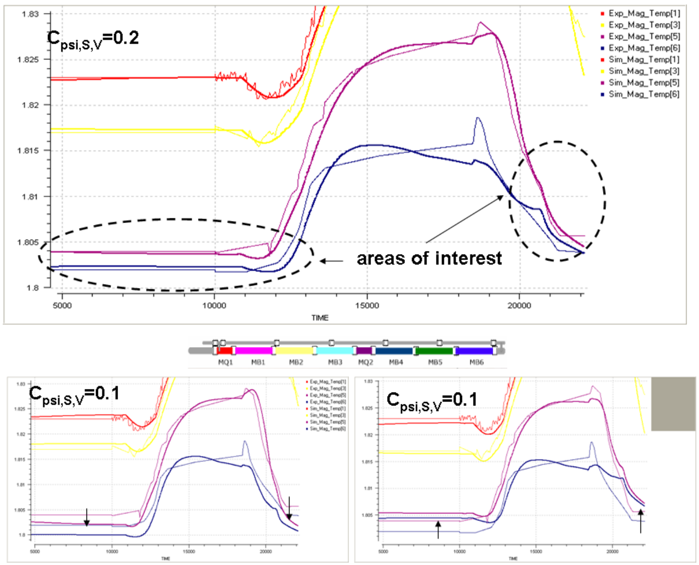

Figure 3.7: Adjusting the pseudo-friction coefficient of the VLP channel of the SHX.

3.5.7 The inertia coefficient $c_{inert,l,F}$

The inertia coefficient $c_{inert,l,F}$ influences the time delay between the helium mass flows at the opposite ends of the FP. The coefficient has been fitted in order to get the delays between the JT valve action and the temperature change of the MB6 dipole close to the experimental data:

$$c_{inert,l,F} = 1200$$

3.5.8 The rangeability of the JT valve

The rangeability of the JT valve determines the JT valve characteristic that is the model control input, thus has a crucial importance for the behavior of the model.

The maximal flow of helium through the JT Valve at lift $x = 1$ was calculated according to the equation 2.49

$$F_{l,v,J}(1) = 23.7[g/s] \tag{3.3}$$

The relation $F_{l,v,J} = f(x)$ at constant pressure drop along the JT valve has the form

$$F_{JT} = x * R^{x-1} \tag{3.4}$$

The rangeability R has been found substituting the experimental values of F_{JT} and x, coming from the calibration curve of the JT valve, in the equation above. I have found

$$R = 68$$

With this value of the rangeability the valve characteristic looks like in the figure 3.8

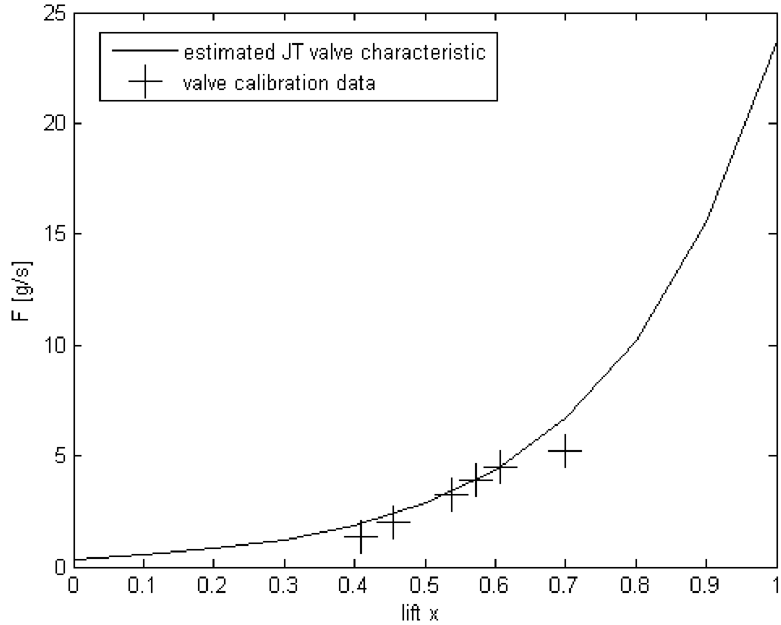

Figure 3.8: Estimated JT valve flow characteristic.

3.6 Model Validation

The model has been validated with available data from 4 experiments performed on the String2 prototype.

3.6.1 JT Valve manipulation experiment

The results of the model simulation in the "nominal3" experiment are very good.

Shape, timing and amplitudes of the simulated values of temperatures are very close to the experimental data, see fig 3.9

The results of the model simulation in the "nominal1" experiment are worse the in the previous experiment.

Shape, and timing are all right but amplitudes of the simulated values of temperatures are incorrect, see figure 3.10. This can be cause by different than in the phase3, distribution of static heat loads along the String2 prototype.

3.6.2 Additional heat load experiment

In this experiment the reaction of the model on the additional head load applied into the MQ2 is compared with the experimental data from "hload3" experiment performed on the String2 phase3 prototype.

The results of simulation are very close to the experimental data, see figure 3.11 .

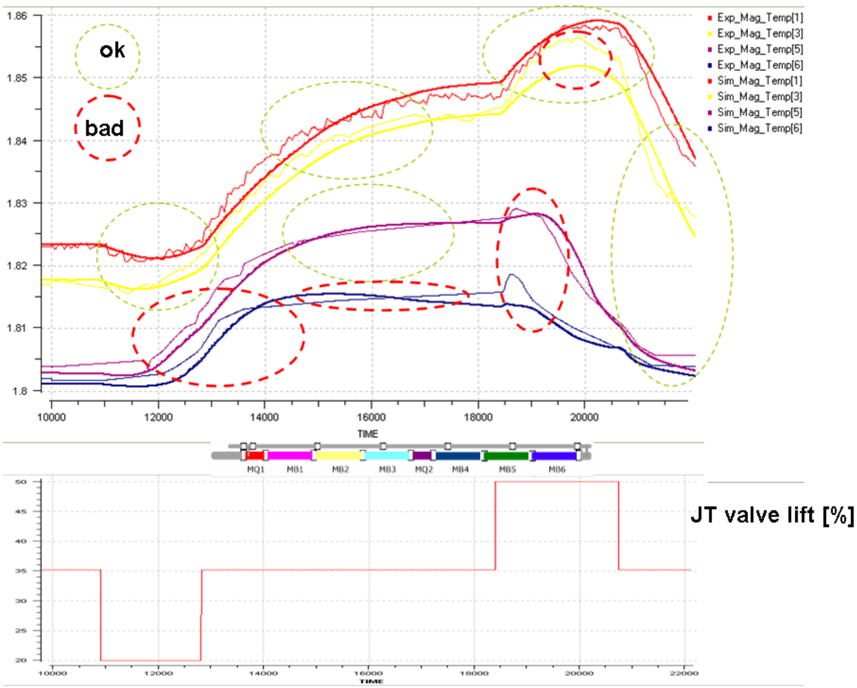

Figure 3.9: Model validation. Experiment "Nominal3"
The thin curves represent experimental data, bold are the simulation results.

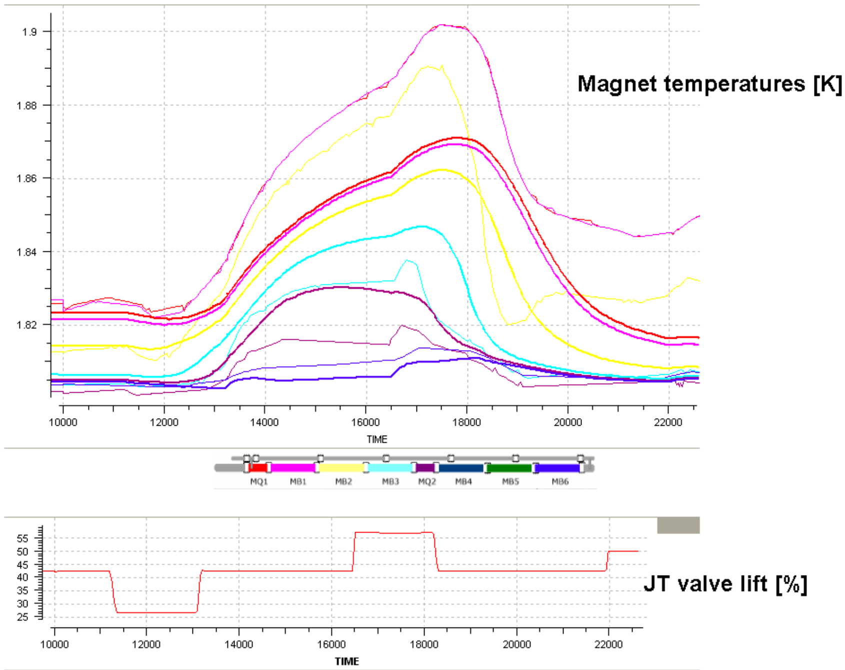

Figure 3.10: Model validation. Experiment "Nominal1"
The thin curves represent experimental data, bold are the simulation results.

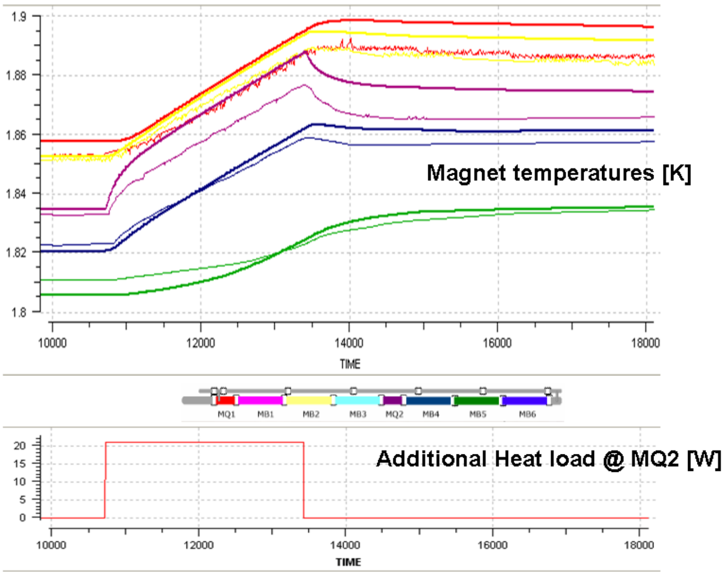

Figure 3.11: Model validation. Experiment "Hload1"
The thin curves represent experimental data, bold are the simulation results.

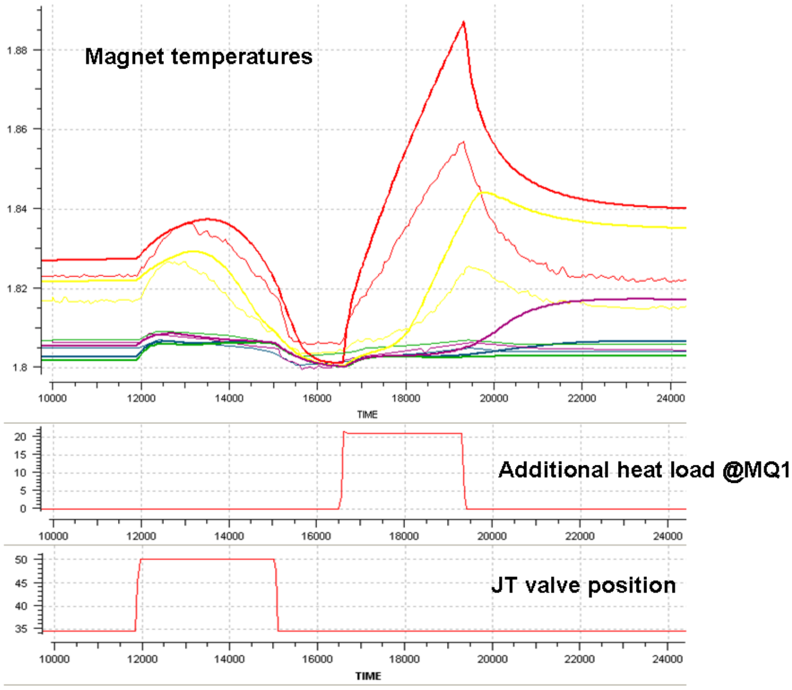

Figure 3.12: Model validation. Experiment "Mixed1"
The thin curves represent experimental data, bold are the simulation results.

3.6.3 Mixed experiment

In this experiment the reaction of the model on theJT valve manipulation and additional head load applied into the MQ2 is compared with the experimental data from "mixed1" experiment performed on the String2 phase3 prototype.

The results of simulation are not exactly close to the experimental data, see figure 3.12 .

3.7 Summary

The model simulation showed that the basic physical principles determining the behavior of the Superfluid Helium Cryogenic Circuit of the Standard Cell are implemented well.

The inverse response of the simulated magnet temperatures on the JT valve manipulation has good shape and amplitude comparing to the measured dynamics of the magnet temperature.

Unfortunately, the model seems not to be accurate for stronger heat loads, see the experiment "nominal1". The reason for this can be the different heat load distribution during the experiment, corresponding to the phase2 configuration of the String2 Prototype.

Finally, the cooling loop has not been closed - the temperature of the supercritical helium arriving to the JT valve has not been modeled and the experimental values has been used during adjusting and validation of the model.

That means that the model is not finished and in this form cannot be used to make the temperature prediction.

The positive observation is that the model in the present form can be simulated relatively fast: the 14000 [s] of an experiment has been simulated in time about 250 [s].

3.8 Future work

There are many activities left to do in order to develop the NMPC for the Superfluid Helium Cryogenic Circuit.

The first task to accomplish is to finish the model, and precisely close the cooling loop - the temperature of the supercritical helium arriving to the JT valve must be modeled.

An investigation of the behavior of the model at higher heat loads is also needed in order to explain the differences observed during simulation of the String2 phase2 prototype.

This lets achieve the starting point for the development of advanced controller for the Superfluid Circuit of a LHC Standard Cell.

Bibliography

[1] http://www.cern.ch/ "What is CERN?" , 2007

[2] http://www.wikipedia.org; "Large Hydron Collider"; 2007

[3] http://www.wikipedia.org; "CERN"; 2007

[4] http://www.wikipedia.org; "Superconductivity"; 2007

[5] M. Chorowski et al. "A proposal for simplification of the LHC cryogenic schema", Adv. Cryog. Eng., A : 43 (1998) , pp.395-402

[6] Enrique Blanco "Nonlinear Model-based Predictive Control Applied To Large Scale Cryogenics Facilities", PhD thesis, Universidad de Valladolid, 2001

[7] M. Chorowski et al. "A Simplified Cryogenic Distribution Scheme for the Large Hadron Collider", LHC Project Report 143, 1997

[8] Rolf Findeisen, Frank Allgöwer "An Introduction to Nonlinear Model Predictive Control"

[9] Empresarios Agrupados International; "EcosimPro 4 User Guide", 2007

[10] B. Flemster "Investigation, Modelling and Control of the 1.9 K Cooling Loop for Superconducting Magnets for the Large Hadron Collider", PhD thesis, 2000

[11] Jrn Andersen "Temperaturregulering ved CERNS Large Hadron Collider", MSc thesis, 2002

[12] CRYODATA, INC. "USER's GUIDE to HEPAK", Version 3.4, January 1999

[13] T. Flynn "Cryogenic Engineering", 1997

[14] L. Bottura,C. Rosso "Finite element simulation of steady state and transient forced convection in superfluid helium", 1999

[15] S.W. Van Sciver "Helium Cryogenics", Clarendon Press, Oxford, 1986

[16] C.J. Gorter and J.H. Mellink "On the irreversible processes in liquid helium II" Physica, 15, p. 285304,1949

[17] N. Bourcey et al. "Final design and experimental validation ot the thermal performance of the LHC lattice cryostats", LHC Project Report 689, 2004

[18] E. Blanco et al. "EXPERIMENTAL VALIDATION AND OPERATION OF THE LHC TEST STRING 2 CRYOGENIC SYSTEM", LHC Project Report 681, 2003

[19] M. Chorowski et al. "A proposl for simplifiction of theLHC Cryogenic Scheme", LHC Project Note 106, 1997

[20] D. Camacho et al. "Thermal Characterization of the HeII LHC Heat Exchanger Tube", LHC Project Report 232, 1998

[21] Ph. Lebrun "Cooling Strings of Superconducting Devices below 2 K: The Helium II Bayonet Heat Exchanger", LHC Project Report 144, 1997

[22] R.J. Donnelly, C.F. Barenghi "The observed Properties of Liquid Helium at the Saturated Vapor Pressure", http://www.darkwing.uoregon.edu/~rjd/, 2004

[23] E. Blanco "Superfluid Helium Cooling Loop on String2", LHC Internal Note, CERN, 2003

[24] N. Gilber et al. "Performance assesment of 239 series helium sub-cooling heat exchanger for the Large Hydron Collider", LHC Project Report 860, 2005

[25] O.Capatina et al. "The Thermal Design and Performance of the Electrical Feed Box of the LHC Prototype Cell", 19th International Cryogenic Engineering Conference, July 2002, Grenoble, France

[26] E. Ödlund "Virtual instrumentation: Introduction of virtual flow meters in the LHC cryogenics control system", MSc thesis, Linköpings Universitet, 2007

[27] "LHC Design Report, Chapter 11 - Cryogenics", CERN

[28] Saban et al. "First results and status of the LHC Test String2", EPAC 2002, Paris, France

Appendix A

Background calculations

A.1 Calculation of the position of the temperature sensors

The position of the temperature sensors was found knowing that the 106.9 m long Standard Cell consist of 2 quadropoles nd 6 dipoles of lengths $l_{quadropole} = 6[m]$ and $l_{dipole} = 15[m]$ respectively and the interconnections between them.

The length of interconnections is calculated base on the assumption that is the same all of them:

$$l_{interconnection} = \frac{106.9 - 2l_{quadropole} - 6l_{dipole}}{8} = 0.613[m] \tag{A.1}$$

Position of the first quadropole:

$$x_{magnet;1} = \frac{l_{quadropole}}{2} + \frac{l_{interconnection}}{2} = 3.31[m] \tag{A.2}$$

and position of following magnets:

$$x_{magnet;i} = \sum_{j=1}^{i-1} l_{magnet;j} + (i - \frac{1}{2}) + \frac{l_{magnet;i}}{2} \tag{A.3}$$

where:

$$l_{magnet;i} = \{ \begin{array}{l} 6[m]; i = 1, 5 \\ 15[m]; i = 2, 3, 4, 6, 7, 8 \end{array}$$